SUPPLEMENT A: MICROSTRUCTURAL ANALYSIS METHODS

Thin-sections were scanned using a PetroScan Microscope (Schmatz et al., 2010; Virgo et al., 2016) with a 10x objective under plane-polarized light and 10 different orientations of crossed polarizers. PetroScan, developed between RWTH Aachen University and Fraunhofer Institute for Applied Information Technology (FIT), consists of a high-end polarization microscope equipped with a camera and an automated sample stage, and image post-processing software. It allows digitization of entire rock thin sections at high magnifications and a variety of polarization and illumination conditions. With crossed polarizers, the extinction behaviour of each pixel is extracted from scans taken at several rotation angles and fitted to continuous curves that represent changes in the pixel intensity in a 360° interval following the procedure of Heilbronner and Pauli (1993). High-resolution digital mosaics were used for measuring vein cement grain sizes using PetroScan image processing and analytical software as well as a reference layer that was superposed by images obtained with high-resolution imaging techniques (see below). Full scans of the studied thin sections are available from the authors of this manuscript.

A selected set of uncoated thin sections were imaged with a Cambridge Image Technology Ltd CL8200 Mk5-2 cold-cathode cathodoluminescence (CL) system. Optical-CL imaging conditions were ~15 kV accelerating voltage, 335 μA gun current and 0.003 mBar chamber pressure.

Scanning electron microscope (SEM)-based secondary electron (SE) imaging, backscatter electron (BSE) imaging and energy-dispersive X-ray spectroscopy (EDS) of experimentally fractured and natural vein samples were performed on tungsten-coated thin sections with a Zeiss SUPRA 55 field emission (FE)SEM at the Institute for Structural Geology, Tectonics and Geomechanics, RWTH Aachen University. SE images of fracture surfaces of experimentally broken samples were used for calcite cleavage-plane segmentation. SE image mosaics were obtained at a working distance of 7 mm, accelerating voltage of 3 kV and magnification of 4000x. 8000x magnification was used for detailed imaging of fracture surfaces. Mineral composition of the wall rock was determined from BSE imaging and EDS measurements that were performed at working distances of ~10 mm and accelerating voltages of 15 to 20 kV.

SEM-CL analysis were performed at the Bureau of Economic Geology, Jackson School of Geosciences, The University of Texas at Austin with a Zeiss Sigma High Vacuum FE-SEM equipped with an Oxford X-Max 50 mm^2 Silicon drift detector (SDD), a pole piece-mounted electron backscattered (BSE) detector and a Gatan MonoCL4 system. Carbon-coated samples were imaged at accelerating voltages of 5 kV, 120 mm aperture, 130-150 dwell time, sample currents of ~3.5 nA, and 2048 x 2048 pixel resolutions following the guidelines of Ukar and Laubach (2016). Under these conditions, image smearing caused by phosphorescence was rarely a problem.

Grain size analysis for Figure 3A was performed on 61 veins from 6 thin sections. Input data for the graph are given in the Table DR1. Optical photomicrograph mosaics from the Virtual microscope scans were imported into Fiji/Image J software and measurements were performed using the line measurement tool as depicted in Figure DR1. For each vein the aperture (**A)** was averaged from at least 10 measurements perpendicular to the vein walls, whereas vein crystal width (**W_v)** was obtained by averaging the width of 20-70 crystals, measured along the median line in the veins. Both values were scaled against the average calcite grain diameter in the wall rock (**W_w**) in order to obtain non-dimensional numbers, **D_m** – referring to the scaled vein width and **W** – referring to the scaled crystal width in veins.

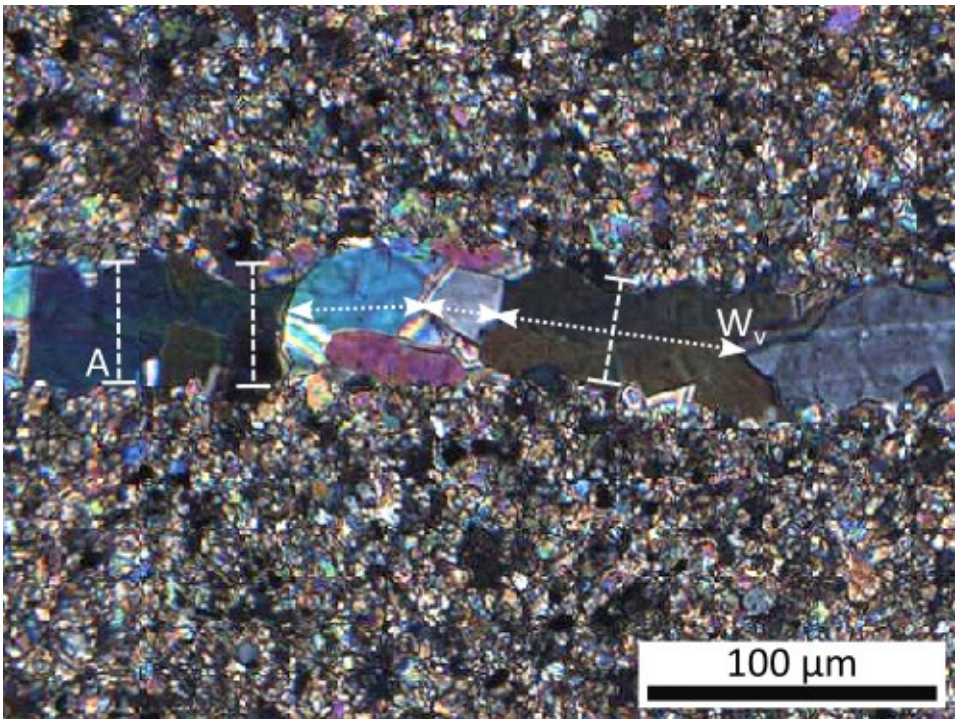

Figure DR1. Example showing how measurements for vein apertures (A) and crystal width in veins (W_v) were performed.

Table DR1. Measurements for Figure 3A. W_v – average crystal width in veins, W – scaled crystal width in veins, A – average vein aperture, D_m – scaled vein aperture

Average calcite grain width in host rock (W_w) = 8 μ					
No.	**Sample**	**W_v (μm)**	**W**	**A (μm)**	**D_m**
1	L4a	86.1	10.8	49.7	6.2
2	L4a	24.1	3.0	15.9	2.0
3	L4a	26.6	3.3	19.3	2.4
4	L4a	52.5	6.6	35.5	4.4
5	L4a	113.7	14.2	59.6	7.5
6	L4a	159.0	19.9	52.8	6.6
7	L4a	102.7	12.8	49.6	6.2
8	L4a	190.4	23.8	63.4	7.9
9	L4a	843.2	105.4	380.0	47.5
10	L4a	613.3	76.7	342.5	42.8
11	L4a	728.5	91.1	1060.1	132.5
12	L4a	449.3	56.2	2437.0	304.6
13	L4a	77.8	9.7	55.0	6.9
14	L4a	24.7	3.1	22.6	2.8
15	L4a	26.9	3.4	25.8	3.2
16	L4a	48.9	6.1	37.4	4.7
17	L4a	257.2	32.1	61.6	7.7
18	L4a	96.9	12.1	44.6	5.6
19	L4a	674.5	84.3	454.7	56.8
20	L4a	257.2	32.1	61.6	7.7
21	L4a	96.9	12.1	44.6	5.6
22	L4a	468.2	58.5	382.1	47.8
23	L4a	522.8	65.3	3785.3	473.2
24	L4b	210.2	26.3	77.8	9.7
25	L4b	49.0	6.1	28.3	3.5
26	L4b	28.0	3.5	21.7	2.7
27	L4b	234.9	29.4	426.2	53.3
28	L4c	380.6	47.6	408.1	51.0
29	L4c	383.6	48.0	245.3	30.7
30	L4c	462.6	57.8	1061.9	132.7
31	L5c	41.5	5.2	42.5	5.3
32	L5c	28.5	3.6	23.1	2.9
33	L5c	31.1	3.9	21.7	2.7
34	L5c	25.5	3.2	24.4	3.1
35	L5c	17.6	2.2	9.9	1.2
36	L5c	38.6	4.8	42.7	5.3
37	L5c	31.7	4.0	28.6	3.6
38	L5c	49.7	6.2	50.3	6.3
39	L5c	24.1	3.0	23.1	2.9
40	L5c	35.9	4.5	34.9	4.4
41	L5c	39.0	4.9	33.3	4.2
42	L5c	41.4	5.2	34.2	4.3
43	L5c	66.7	8.3	49.3	6.2
44	L5c	76.3	9.5	53.8	6.7
45	L5c	238.7	29.8	82.4	10.3
46	L5c	159.4	19.9	74.8	9.4
47	L5c	104.5	13.1	74.0	9.3
48	L5c	97.7	12.2	60.9	7.6
49	L5c	207.7	26.0	90.0	11.2
50	L1c	77.2	9.7	59.8	7.5
51	L1c	45.6	5.7	42.8	5.4
52	L1c	24.9	3.1	27.2	3.4
53	L1c	33.1	4.1	32.7	4.1
54	L1c	95.5	11.9	77.9	9.7
55	L1c	93.1	11.6	60.7	7.6
56	L1c	388.9	48.6	251.1	31.4
57	L1c	201.1	25.1	142.4	17.8
58	L1c	93.4	11.7	39.5	4.9
59	K3c	16.1	2.0	14.1	1.8
60	K3c	22.9	2.9	18.1	2.3
61	K3c	18.9	2.4	15.9	2.0

SUPPLEMENT B: NUMERICAL MODEL

Multiphase-field Model

Crystal growth in calcite veins was modelled using a thermodynamically consistent multiphase-field model (Nestler et al., 2005), which is briefly described in this section. A detailed discussion of the model equations is given in Ankit et al. 2013, Wendler et al. 2016 and Prajapati et al. 2017.

We consider a domain Ω comprising N phase-field order parameters $\phi_\alpha(\mathbf{x},t)$. Each phase-field parameter $\phi_\alpha(\mathbf{x},t) \in [0,1]$ gives the volume fraction of a particular solid or liquid phase at position $\mathbf{x}$ and time t, where the summation constraint $\sum_{\alpha=1}^{N} \phi_\alpha = 1$ is valid at each computational grid point. The order parameters are collectively represented by the phase-field vector $\boldsymbol{\phi}(\mathbf{x},t) = [\phi_1(\mathbf{x},t), \dots, \phi_N(\mathbf{x},t)]$. Each phase-field can be assigned with individual material properties (e.g. crystallographic orientation). A diffuse transition region of finite width characterizes the interface between different phases, in which the magnitude of a phase-field ϕ_α varies smoothly from 1 inside the bulk phase to 0 outside. The length scale parameter ε controls the diffuse interface width.

The temporal evolution of the phase-fields is determined by a local minimization of the Helmholtz free energy, which is given by

$$\mathcal{F}(\boldsymbol{\phi}, \nabla\boldsymbol{\phi}) = \int_\Omega \left[\varepsilon a(\boldsymbol{\phi}, \nabla\boldsymbol{\phi}) + \frac{1}{\varepsilon}\omega(\boldsymbol{\phi}) + f_{\text{bulk}}(\boldsymbol{\phi})\right] \mathrm{d}\Omega = \mathcal{F}_{\text{intf}} + \mathcal{F}_{\text{bulk}}$$

Here, the gradient energy density $\varepsilon a(\boldsymbol{\phi}, \nabla\boldsymbol{\phi})$ and the potential free energy density $\frac{1}{\varepsilon} w(\boldsymbol{\phi})$ represent the interfacial energy density contribution and $f_{\text{bulk}}(\boldsymbol{\phi})$ is the bulk free energy density $f_{\text{bulk}}(\boldsymbol{\phi})$. $\nabla\boldsymbol{\phi}$ denotes the gradient of the phase-field vector $\boldsymbol{\phi}$. The gradient energy density is given by

$$\varepsilon a(\boldsymbol{\phi}, \nabla(\boldsymbol{\phi})) = \varepsilon \sum_{\alpha<\beta}^{N} \gamma_{\alpha\beta}\, a_{\alpha\beta}^2(\boldsymbol{\phi}, \nabla\boldsymbol{\phi}) |q_{\alpha\beta}|^2$$

in which $\gamma_{\alpha\beta}$ is the surface energy density of α-β interface, $\mathbf{q}_{\alpha\beta} = \phi_\alpha \nabla\phi_\beta - \phi_\beta \nabla\phi_\alpha$ denotes the normal vector to the interface, and $a_{\alpha\beta}$ is the anisotropic surface energy function. To model faceted grain growth, the anisotropic surface energy function is piecewise defined as

$$a_{\alpha\beta}(\boldsymbol{\phi}, \nabla\boldsymbol{\phi}) = \max_{1\le k\le n_{\alpha\beta}} \{\hat{\mathbf{n}} \cdot \eta_{k,\alpha\beta}\}$$

where $\hat{\mathbf{n}} = \frac{\mathbf{q}_{\alpha\beta}}{|\mathbf{q}_{\alpha\beta}|}$ is the unit normal vector and $\{\eta_{k,\alpha\beta} | k = 1, \dots, n_{\alpha\beta}\}$ are the $n_{\alpha\beta}$ corners of the Wulff shape of the α-β interface. The multi-obstacle potential energy density is given by

$$\frac{1}{\varepsilon} w(\boldsymbol{\phi}) = \begin{cases} \frac{16}{\varepsilon\pi^2} \sum_{\alpha<\beta}^{N} \gamma_{\alpha\beta}\, \phi_\alpha \phi_\beta + \sum_{\alpha<\beta<\delta}^{N} \gamma_{\alpha\beta\delta}\, \phi_\alpha \phi_\beta \phi_\delta & \text{if } \boldsymbol{\phi} \in \mathcal{G} \\ \infty & \text{else} \end{cases}$$

with the Gibbs simplex $\mathcal{G} = \{\boldsymbol{\phi} | \sum_\alpha \phi_\alpha = 1, \text{and } \phi_\alpha \ge 0\}$. The second term reduces the occurrence of unphysical higher order phases in binary interfaces. Further, the bulk free energy density is linearly interpolated in a diffuse interface region $f_{\text{bulk}}(\boldsymbol{\phi}) = \sum_\alpha^N \phi^\alpha f_{\text{bulk}}^\alpha$. With the variational derivative of the energy functional the evolution of each phase-field ϕ_α reads as (Steinbach, 2009)

$$\frac{\partial \phi_\alpha}{\partial t} = -\frac{1}{N\varepsilon} \sum_{\alpha\neq\beta}^{N} \left[M_{\alpha\beta}(\hat{\mathbf{n}}) \left(\frac{\delta \mathcal{F}_{\text{intf}}}{\delta \phi_\alpha} - \frac{\delta \mathcal{F}_{\text{intf}}}{\delta \phi_\beta} - \frac{8\sqrt{\phi_\alpha \phi_\beta}}{\pi} \left(\frac{\delta \mathcal{F}_{\text{bulk}}}{\delta \phi_\beta} - \frac{\delta \mathcal{F}_{\text{bulk}}}{\delta \phi_\alpha} \right) \right) \right]$$

where the mobility $M_{\alpha\beta}(\hat{\mathbf{n}})$ of the α-β interface is given by

$$M_{\alpha\beta}(\hat{\mathbf{n}}) = M_{\alpha\beta}^0 a_{\alpha\beta}^{\text{kin}}(\hat{\mathbf{n}}).$$

$M_{\alpha\beta}^0$ denotes the kinetic coefficient and $a_{\alpha\beta}^{\text{kin}}(\hat{\mathbf{n}})$ is the kinetic anisotropy. With this approach the mobility is not interpolated, which allows the use of different mobilities for different phases and prevents unphysical retarded movement of solid-solid-liquid triple points. We follow the approach of Wendler et al. (2016) for modelling a faster growth rate of rough non-equilibrium crystal surfaces and decreased growth velocity after crystal facets have formed (Lander et al., 2008) and use

$$a_{\alpha\beta}^{kin}(\hat{\mathbf{n}}) = \left(1+\delta\left(\max_k\{\hat{\mathbf{n}}\cdot\eta_{k\alpha\beta}\}-\max_{k-1}\{\hat{\mathbf{n}}\cdot\eta_{k\alpha\beta}\}\right)\right)\max_k\{\hat{\mathbf{n}}\cdot\eta_{k\alpha\beta}\}$$

for kinetic anisotropy. Here $\max_k\{\dots\}$ gives the largest and $\max_{k-1}\{\dots\}$ the second largest argument of the scalar products. When the crystal is in a non-equilibrium shape the largest and second largest argument differ, whereas in equilibrium shape $\max_k\{\dots\}$ and $\max_{k-1}\{\dots\}$ are equal and the second argument vanishes.

The multiphase-field model equations are implemented in the PACE3D software package (version 2.5.1), which is written in language C. The evolution equations for the phase fields are solved on an equidistant orthogonal computational grid using an explicit Euler scheme for the temporal derivative and central difference scheme for the spatial derivatives. A locally reduced order parameter optimization (LROP) is applied to reduce computational costs, where the evolution equation is only solved for the locally present phases. The parameters used in the presented simulations are given in Table DR2. The simulation parameters are chosen in order to obtain a numerically stable simulation, to reduce the computational costs and to reproduce the microscopic/natural observations of the calcite veins. Therefore, the simulation results give information about the kinematics of vein growth. With additional physical properties (e.g. pressure, temperature, supersaturation) at hand a mapping of the non-dimensional simulation parameters is possible to get additional information about the growth kinetics (see e.g. approach of Wendler et al., 2016 and Prajapati et al., 2020 for quartz cementation). In the presented simulations we use a constant chemical driving force f_{bulk}^{α} which assumes continuous inflow of constant supersaturated fluid and slow attachment kinetics compared to flow rate.

Table DR2. Values of phase-field model parameters used in simulations

Model parameter	Value
Grid spacing Δx	1
Time-step width Δt	0.035
Length scale parameter ε	6.5
Interfacial energy density $\gamma_{\alpha\beta}$	1.0
Higher order parameter $\gamma_{\alpha\beta\delta}$	20.0
Mobility of transgranular fractured grains to liquid $M^0_{\text{intra. gr, liq}}$	1.0
Mobility of intergranular fractured grains to liquid $M^0_{\text{inter. gr, liq}}$	0.05-1
Mobility of inert grains (e.g. silica) to liquid $M^0_{\text{inert, liq}}$	0
δ	1.0
Bulk energy density for crystals f_{bulk}^{α}	-0.25 (2D) / -0.5 (3D)

The 2D computational domain is set up with a grid size of 2500 cells in the x direction and 145, 159, 166, 174, 204, 262, 321, and 380 cells in the y direction for apertures of 0.5, 1, 1.5, 2, 4, 8, 12, and 16 Dm respectively. We scale the vein aperture to the average grain diameter of the wall-rock and refer to it as parameter "Dm". The simulation setup with the applied boundary conditions is depicted in Figure DR2A. An *isolated*/zero-gradient boundary condition is set at the upper and lower boundary. At the right and left boundary an *anisotropic* boundary condition is applied, which ensures that the shape of the crystal facets is maintained precisely.

The simulation setup in 3D comprises 599 cells in the x direction, 250 cells in the zdirection, and 80, 116, and 279 cells in the y direction for apertures of 2, 4, and 8Dm respectively. The boundaries normal to the y direction are set to *isolated*, where an anisotropic boundary condition is applied at the faces normal to the x and z directions. Figure DR2C depicts the simulation setup for an aperture of 4 Dm.

Simulation Setup and Boundary Conditions

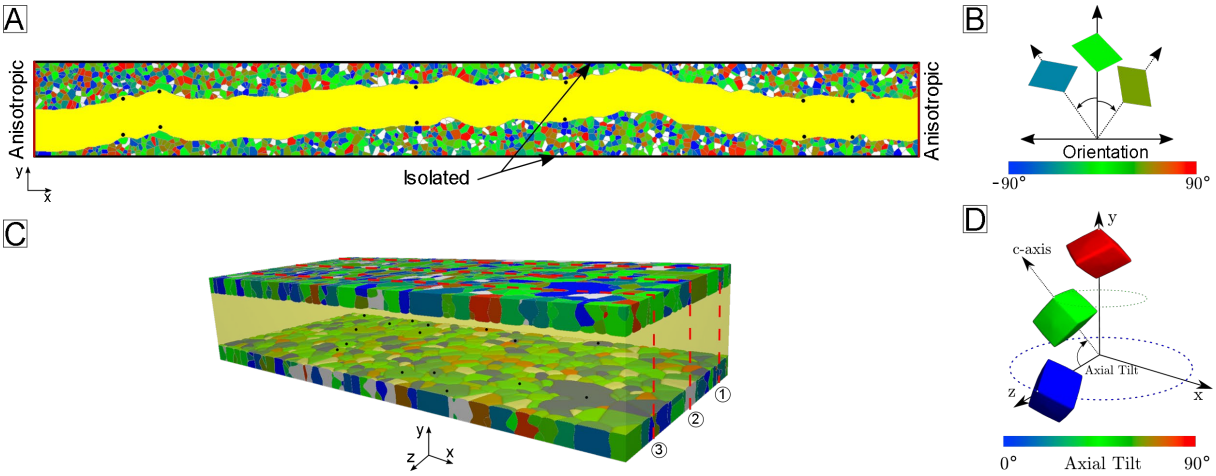

Figure DR2. A - 2D Simulation setup of an aperture of 8 D_m depicting the applied boundary conditions. The fracture is filled with a liquid phase (in yellow) and inert grains in respect to calcite precipitation (e.g. quartz, feldspar, clay) are marked in light grey. Intergranular fractured grains (mirrored) are marked with black dots; B - Color bar indicates the orientation of the rhombohedral calcite grains in the wall rock in A; C – 3D Simulation setup with a liquid phase (yellow) and inert grains (light grey). Intergranular fractured grains (see Figure 2D) are marked with black dots. Periodic boundary conditions are applied for the phase-field simulations in the x and z directions. The cross-sectional planes, depicted in Supplement D are indicated by ①, ②, and ③; D – Color bar for the 3D Setup in C indicates the axial tilt of the rotated rhombohedral calcite grains.

The initial structure of the wall rock is generated with a Voronoi algorithm, where the crystal orientation of the grains is set randomly. Then the mirrored transgranular fractured grains

along different Profile lines (in 2D) or Profile area (in 3D) (Figure DR2D) are combined with the wall rock structure, generated by Voronoi algorithm. Black dots in the setups indicate the transgranular fractured grains. The proportions of transgranular vs intergranular vs inert surfaces for each 2D Profile lines are depicted in Table DR3.

Table DR3. Proportions of fracture surface types along the profile lines in Figure 2D that were used in 2D simulations

Transgranular cracks	17.5%	9.8%	7.5%	5.6%
Intergranular cracks	72.9%	79.8%	81.8%	83.6%
Inert surface	9.6%	10.4%	10.7%	10.8%

The faster growth of transgranular fractured grains is modelled by increasing the mobility of transgranular fractured grains along cleavage planes $M^0_{\text{intra. gr, liq}}$ compared to the mobility of intergranular segment boundaries $M^0_{\text{inter. gr, liq}}$, where the factor $\xi = M^0_{\text{intra. gr, liq}} / M^0_{\text{inter. gr, liq}}$ gives the ratio of the different mobilities. Grain boundaries are assumed to be immobile by setting the mobility of solid-solid interfaces to zero. Therefore, grain growth only occurs at solid/liquid interfaces. Moreover, the mobility of inert segments (e.g. feldspar grains) is also set to zero $M^0_{\text{inert, liq}} = 0$.

In our simulations, we chose rhombohedral crystal habit for calcite grains because this is the most common in nature. We utilized the same vertices for the anisotropy formulation of the gradient energy density and the mobility. The equilibrium crystal shape for the right-hand projection of rhombohedral calcite in 2D (Prajapati et al., 2018) and the 3D shape are depicted in Figures DR2B and D, respectively.

Simulation results for the 2D structure are presented in *Supplement C* and *Multimedia Supplement*. Results for the 3D simulations are presented in *Supplement D*.

Fluid Flow

We extract the sharp interface data from the diffuse phase-field simulations and use this microstructure as an input for fluid flow simulations in PACE3D. Incompressible stationary Stokes equations without body forces are solved assuming low flow velocities in the simulated domain (Reynolds number $Re \ll 1$). The conservation of mass and linear momentum is given by

$$\mu\Delta\mathbf{u} - \nabla p = 0,$$
$$\nabla \cdot \mathbf{u} = 0,$$

where $\mathbf{u}$ is the fluid velocity, μ denotes the dynamic viscosity, and ∇p is the pressure gradient.

We apply a pressure drop on the boundaries normal to the z-direction and set periodic boundaries in the x direction (see Figure DR2D). A no-slip condition is prescribed for the liquid-solid interfaces, where the velocity is set to $\mathbf{u}_{\text{sol-liq}} = \mathbf{0}$. The chosen simulation parameters are given in Table DR4.

We visualize the results of the fluid flow simulation with velocity streamlines in our in-house visualization tool *glviewer*. For a stationary flow, the streamlines indicate the pathways of fluid particles in the flow field. The colors of the streamlines represent the velocity magnitude and therefore indicate the permeability of the cemented structure. The velocity magnitude is given as a non-dimensional quantity. with physical properties of the fluid (e.g. density, viscosity) in hand, the physical flow velocity can be computed.

Table DR4. Values of parameters used in fluid-flow simulations

Model parameter	Value
Dynamic viscosity μ	0.9087
Density ρ	1
Pressure drop	2×10^{-4}
Reynolds number Re	0.01

References cited

Ankit, K., Nestler, B., Selzer, M., and Reichardt, M., 2013, Phase-field study of grain boundary tracking behavior in crack-seal microstructures: Contributions to Mineralogy and Petrology, v. 166, p. 1709–1723, https://doi.org/10.1007/s00410-013-0950-x.

Heilbronner, R.P., and Pauli, C., 1993, Integrated spatial and orientation analysis of quartz c-axes by computer-aided microscopy: Journal of Structural Geology, v. 15, p. 369–382, doi:10.1016/0191-8141(93)90133-U.

Lander, R.H., Larese, R.E., and Bonnell, L.M., 2008, Toward more accurate quartz cement models: The importance of euhedral versus noneuhedral growth rates: AAPG Bulletin, v. 92, p. 1537–1563, doi:10.1306/07160808037.

Nestler, B., Garcke, H., and Stinner, B., 2005, Multicomponent alloy solidification: Phase-field modeling and simulations: Physical Review E - Statistical, Nonlinear, and Soft Matter Physics, v. 71, p. 1–6, doi:10.1103/PhysRevE.71.041609.

Prajapati, N., Abad Gonzalez, A., Selzer, M., Nestler, B., Busch, B., and Hilgers, C., 2020, Quartz Cementation

in Polycrystalline Sandstone: Insights From Phase-Field Simulations: Journal of Geophysical Research: Solid Earth, v. 125, p. 1–23, doi:10.1029/2019jb019137.

Prajapati, N., Selzer, M., and Nestler, B., 2017, Computational modeling of calcite cementation in saline limestone aquifers: a phase-field study: Geothermal Energy, v. 5, p. 1–18, doi:10.1186/s40517-017-0072-1.

Prajapati, N., Selzer, M., Nestler, B., Busch, B., and Hilgers, C., 2018, Modeling fracture cementation processes in calcite limestone: a phase-field study: Geothermal Energy, v. 6, doi:10.1186/s40517-018-0093-4.

Schmatz, J., Urai, J.L., Bublat, M., and Berlage, T., 2010, Petro-Scan - Virtual Microscopy, *in* EGU General Assembly.

Steinbach, I., 2009, Phase-field models in materials science: Modelling and Simulation in Materials Science and Engineering, v. 17, doi:10.1088/0965-0393/17/7/073001.

Virgo, S., Heup, T., Urai, J.L., and Berlage, T., 2016, Virtual Petrography (VIP) - A virtual microscope for the geosciences, *in* EGU General Assembly.

Wendler, F., Okamoto, A., and Blum, P., 2016, Phase-field modeling of epitaxial growth of polycrystalline quartz veins in hydrothermal experiments: Geofluids, v. 16, p. 211–230, doi:10.1111/gfl.12144.

SUPPLEMENT C: 2D RESULTS

Table DR5. Values of data points from phase-field simulations that are represented in the Figure 3A. The percentages in the setup row refers to the percentage of transgranular segments on the fracture surface.

Setup	17.5%; ξ= 5	9.8%; ξ=12	7.5%; ξ=11	5.6%; ξ=20
Aperture	Av Gs Size	Av Gs Size	Av Gs Size	Av Gs Size
0.5	0.94	0.89	0.88	0.84
1	1.15	1.19	1.00	1.10
1.5	1.34	1.43	1.24	1.31
2	1.61	1.74	1.61	1.66
4	3.31	5.63	4.22	5.28
8	14.08	21.11	21.11	28.15
12	16.89	21.11	28.15	33.78
16	16.89	21.11	28.15	33.78

The temporal evolution of the vein microstructures for apertures of 1, 2, 4, 8, 12, and 16 Dm with a hindering factors (ξ) of 1 (no hindering), 5, and 20 (transgranularly fractured grains grow 20x faster than intergranularly fractured grains) is given in the following figures.

All following simulations are performed using profile line with 17.5% transgranular segments that are assigned fast growth rates (Fig. 2D).

Fracture aperture 1 Dm;

ξ=1

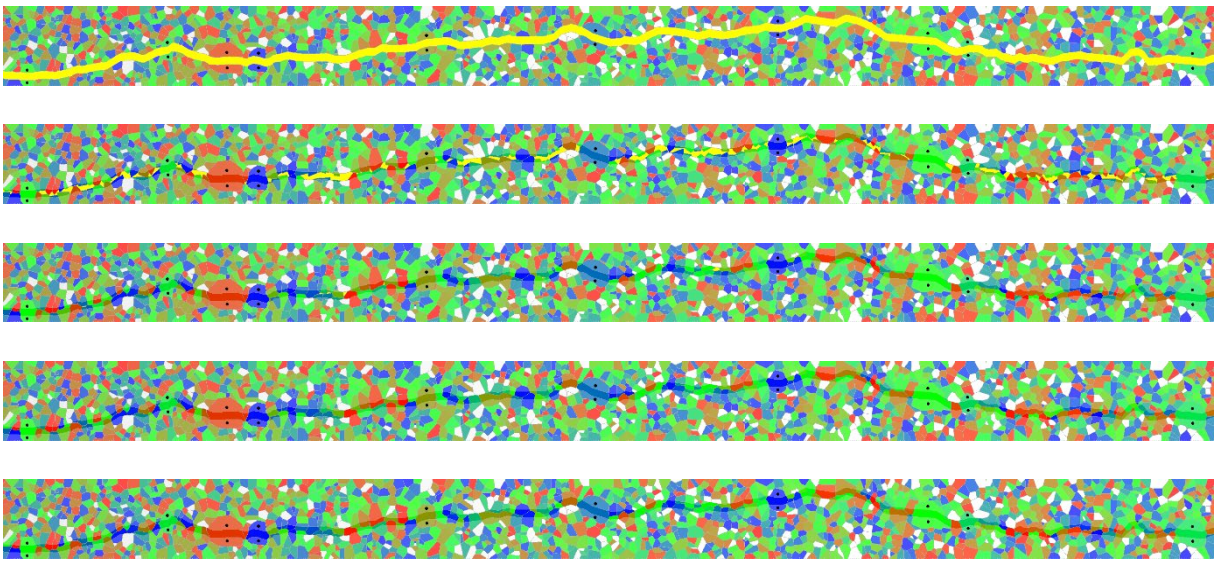

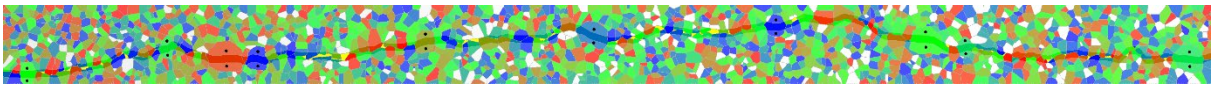

Fracture aperture 2 Dm; ξ=1

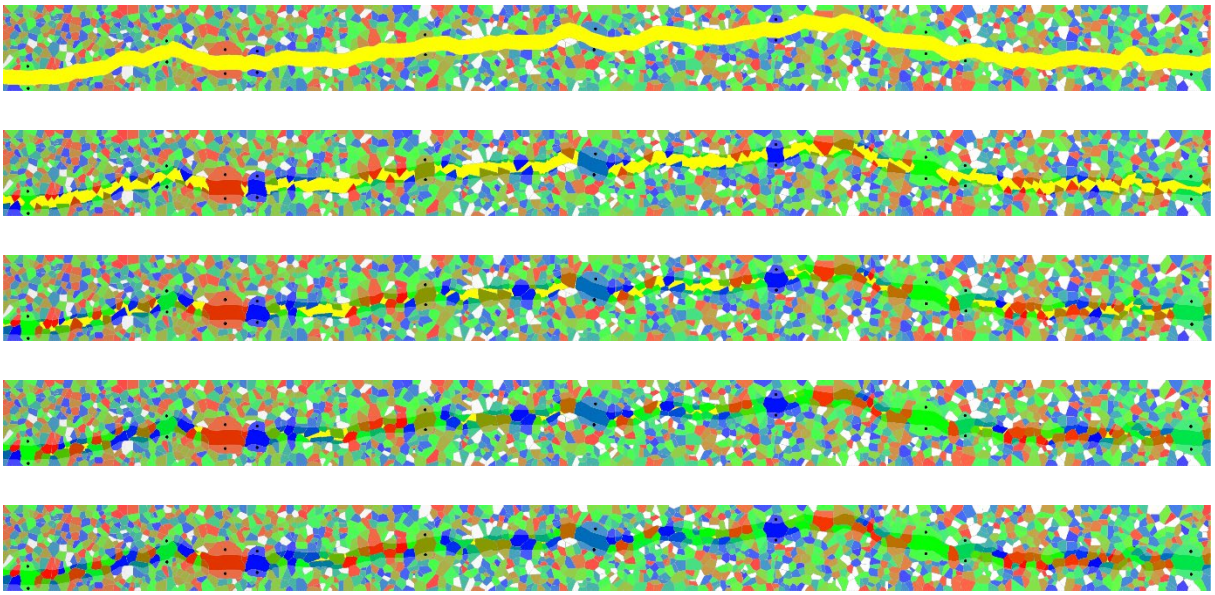

Fracture aperture 4 Dm; ξ=1

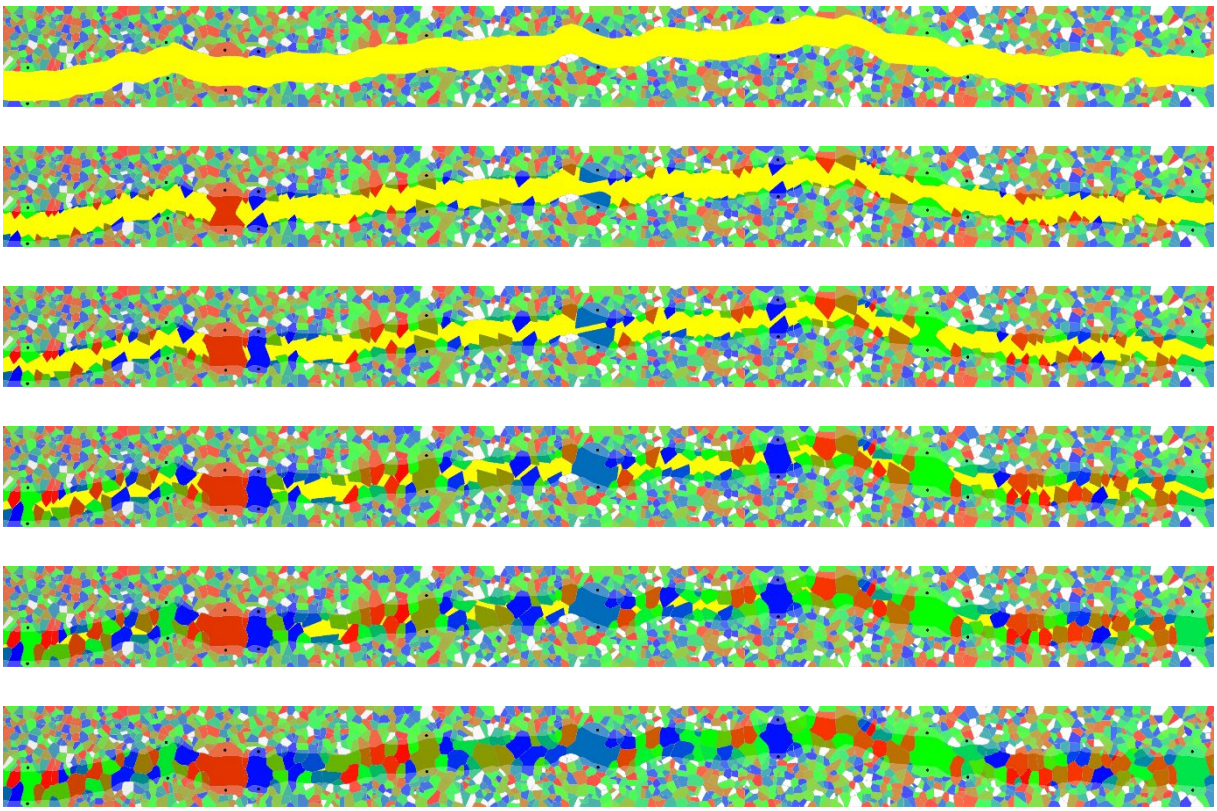

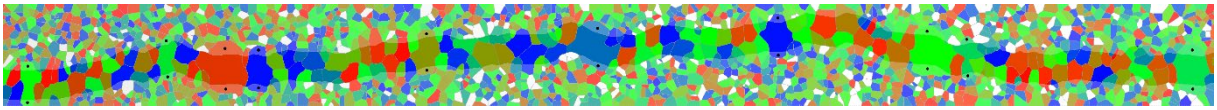

Fracture aperture 8 Dm; ξ=1

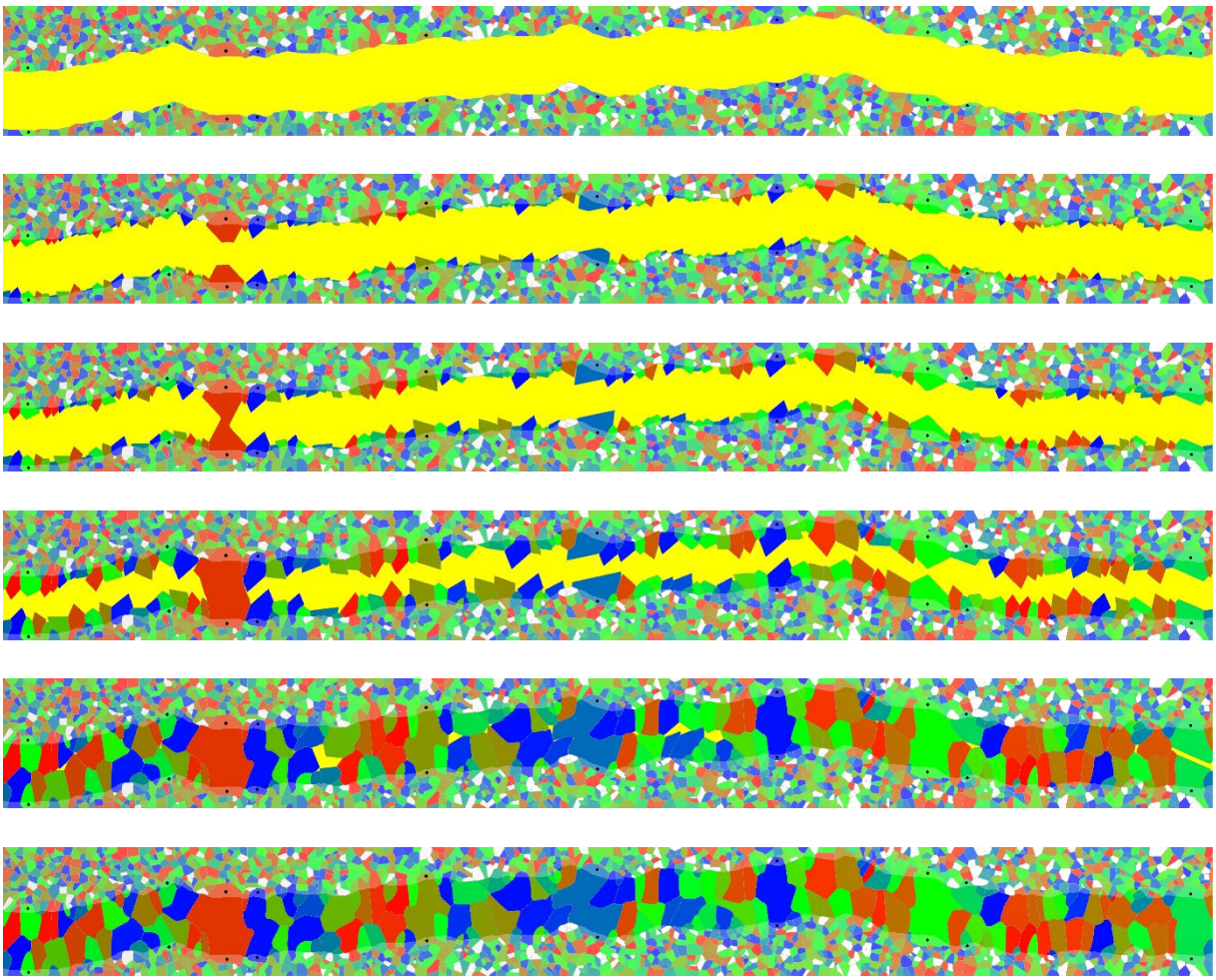

Fracture aperture 12 Dm; ξ=1

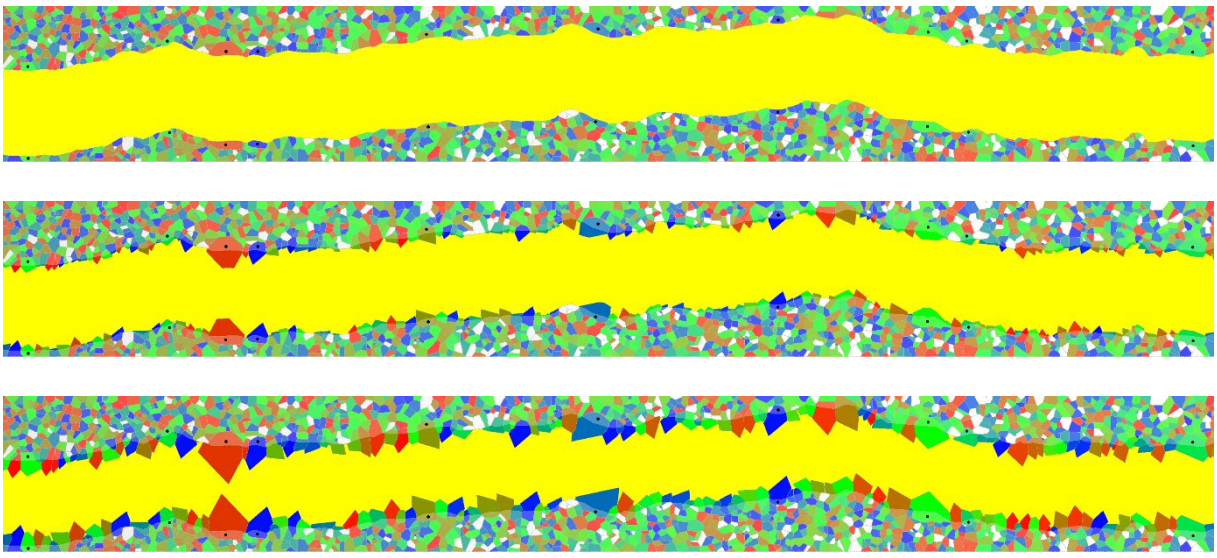

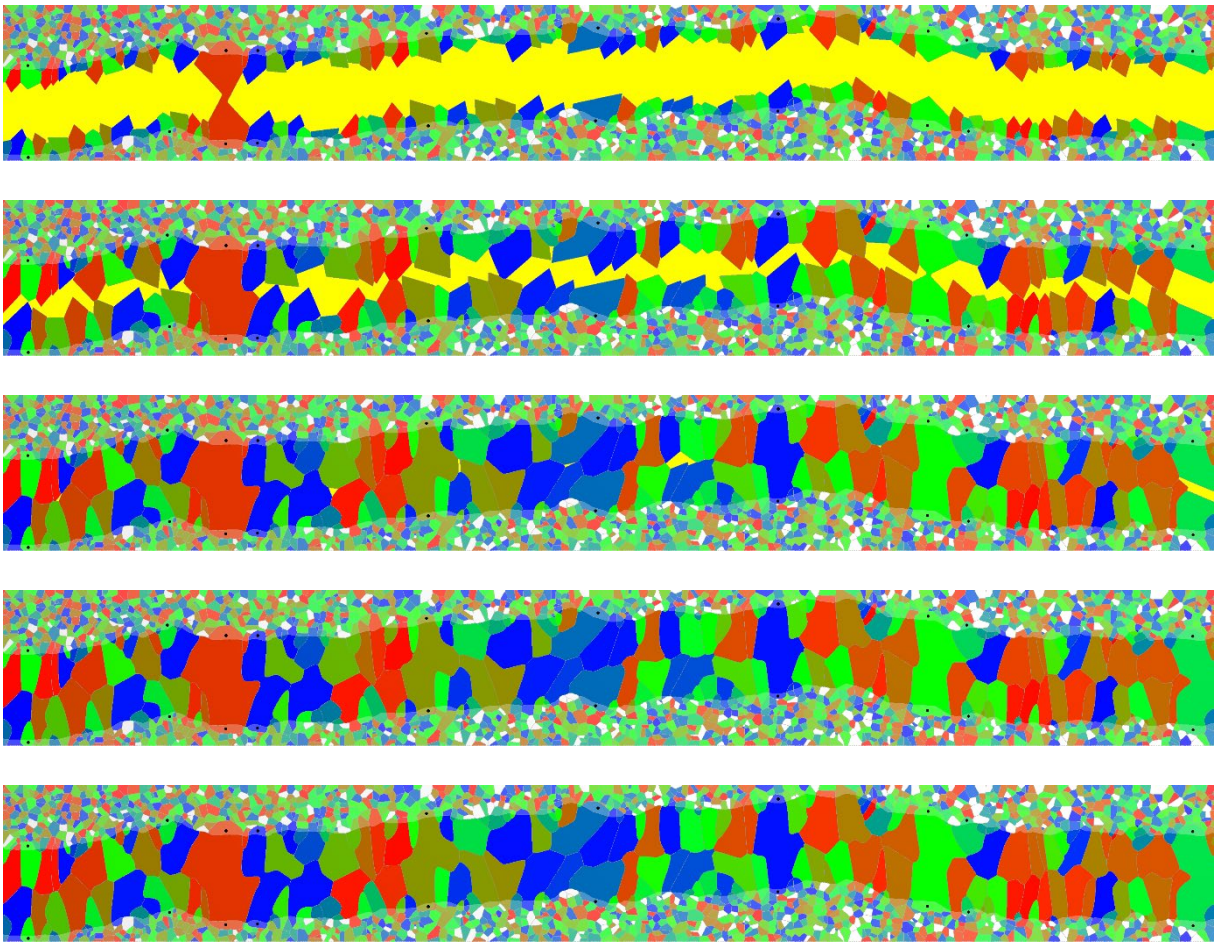

Fracture aperture 16 Dm; ξ=1

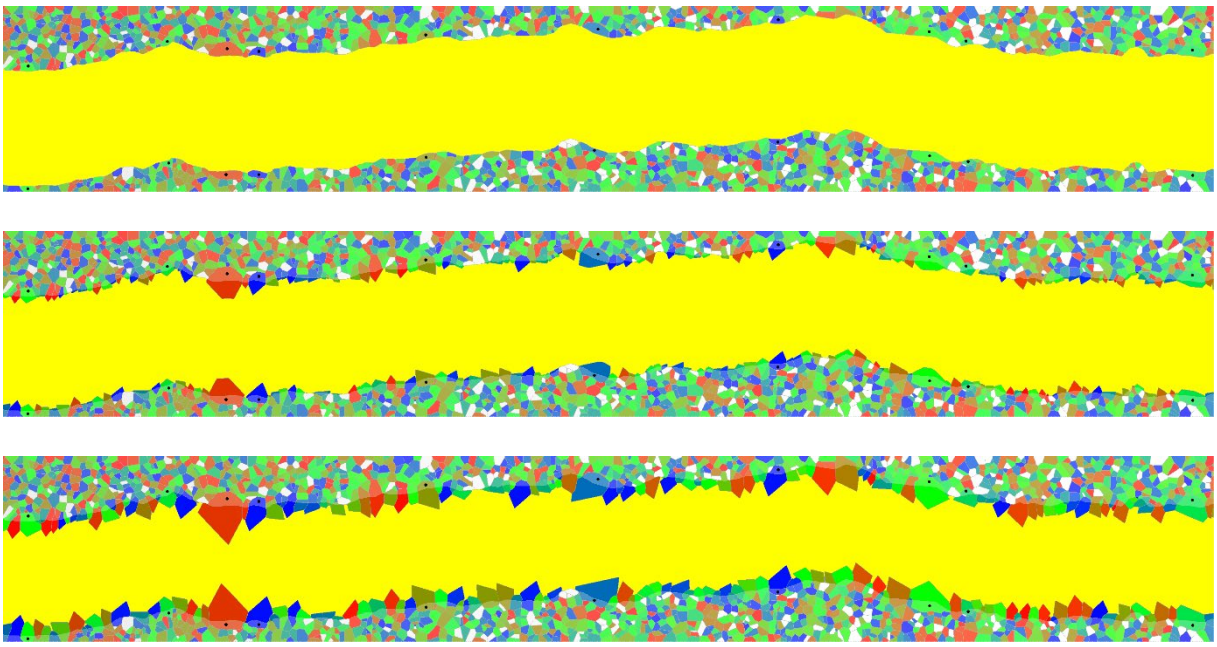

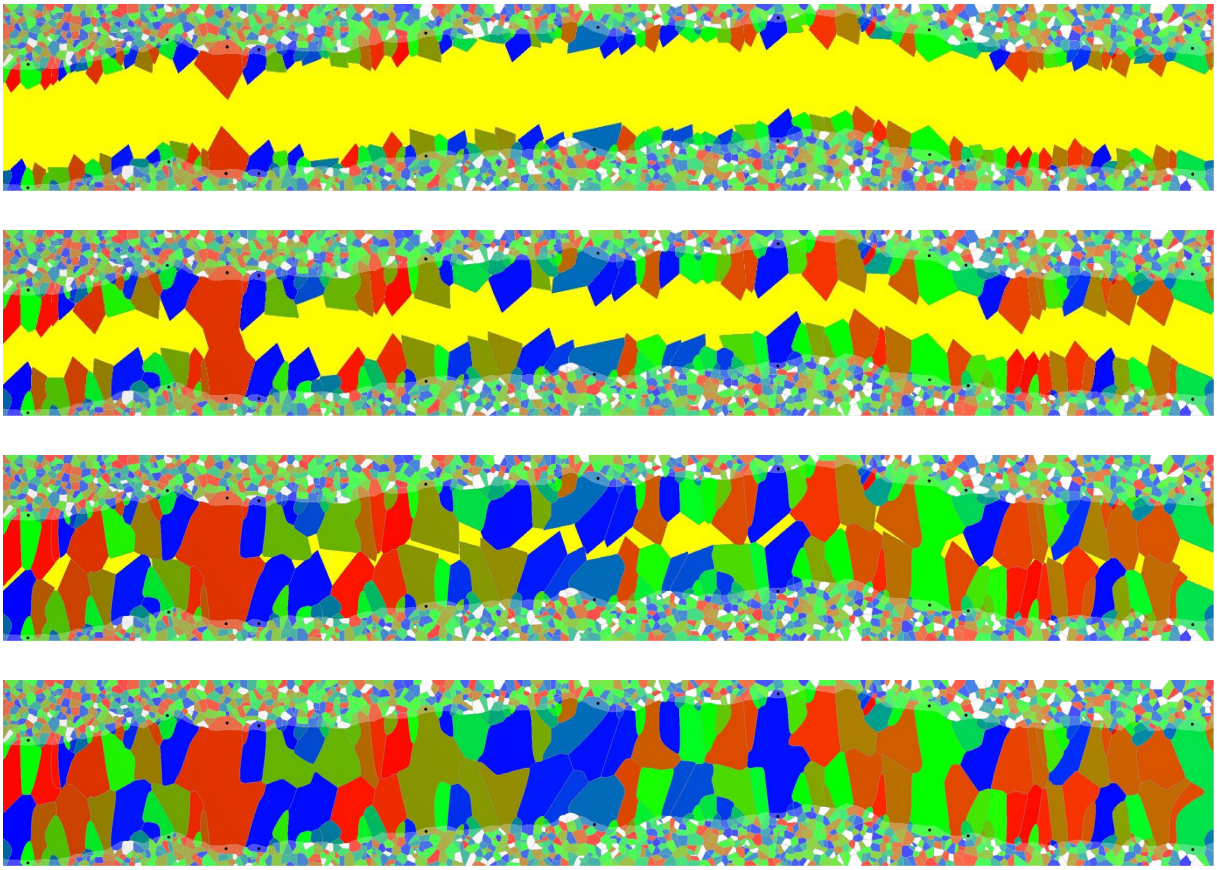

Fracture aperture 1 Dm; ξ=5

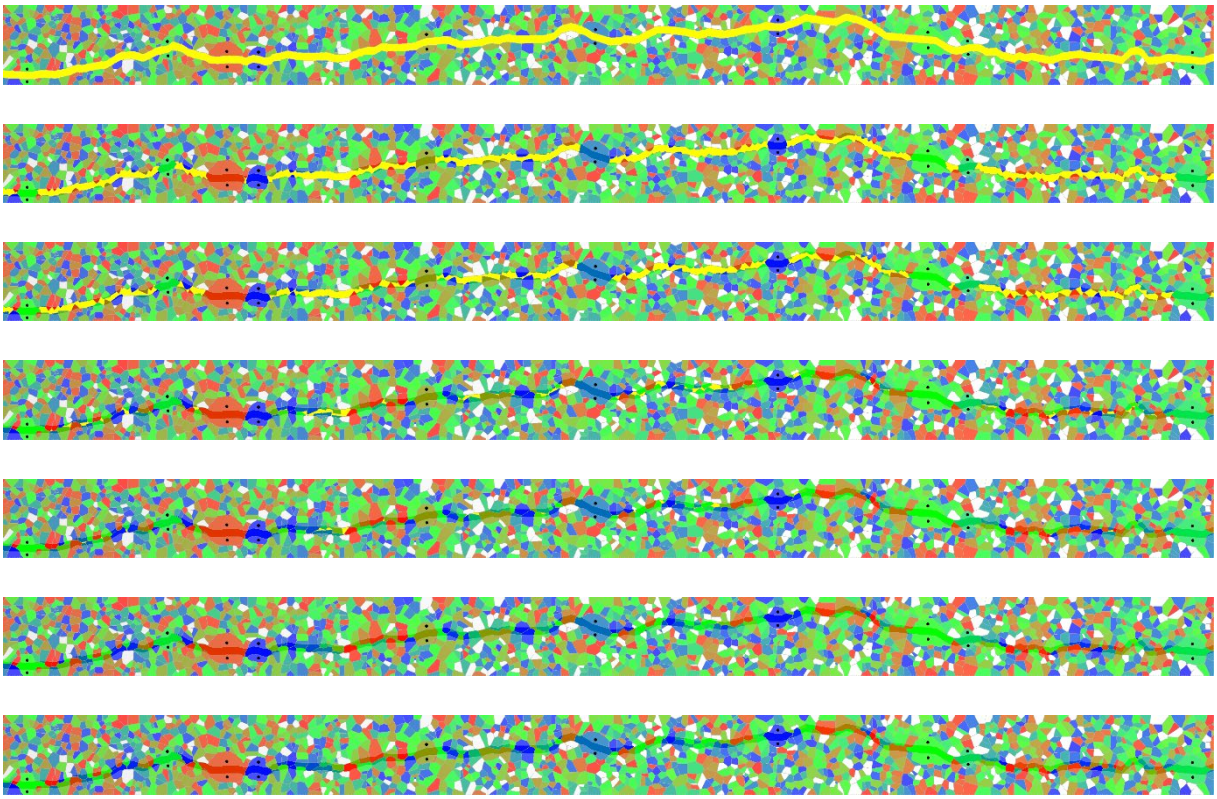

Fracture aperture 2 Dm; ξ=5

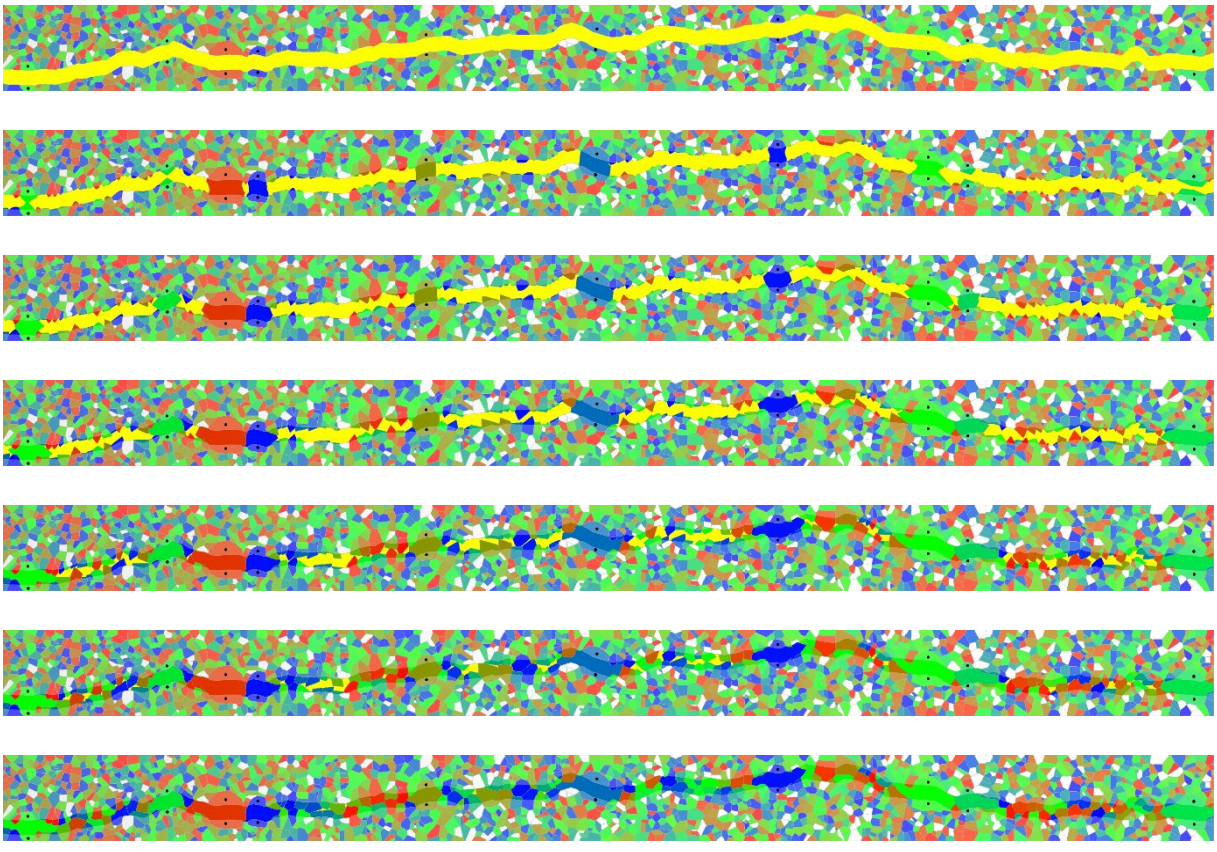

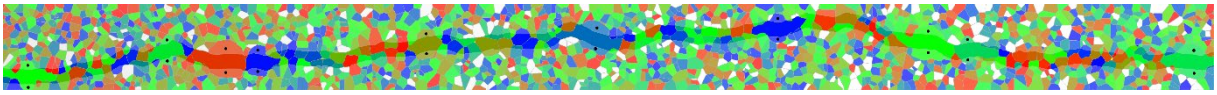

Fracture aperture 4 Dm; ξ=5

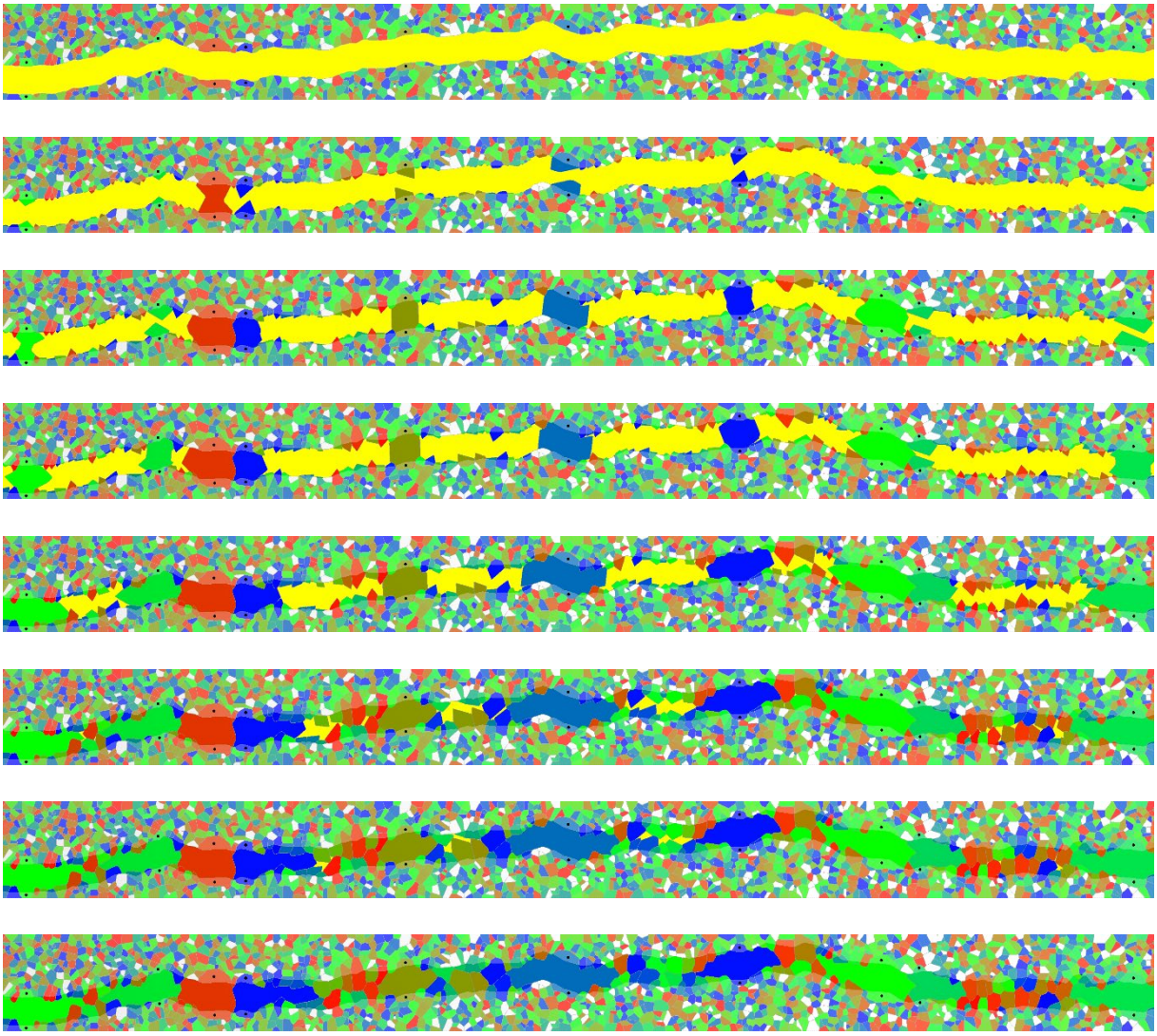

Fracture aperture 8 Dm; ξ=5

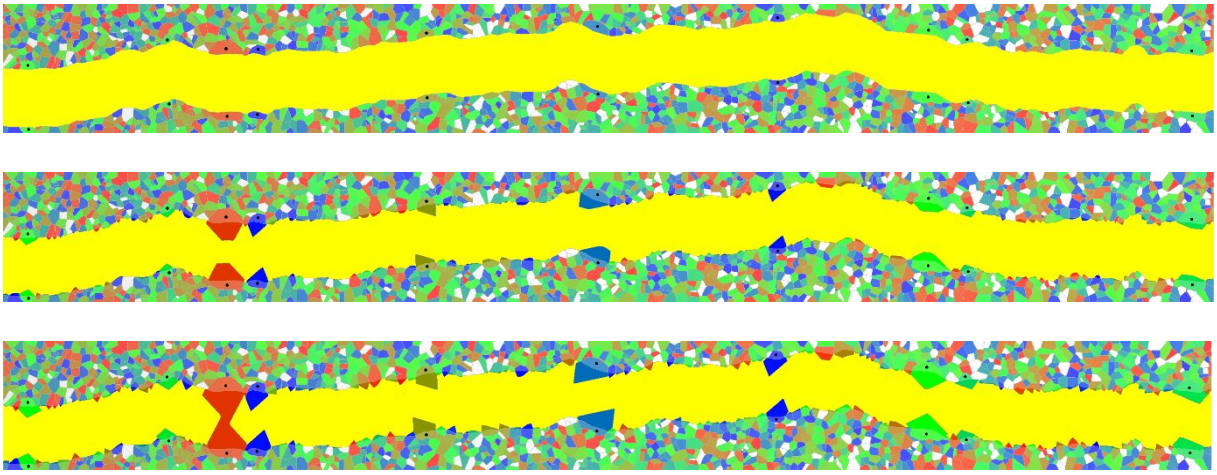

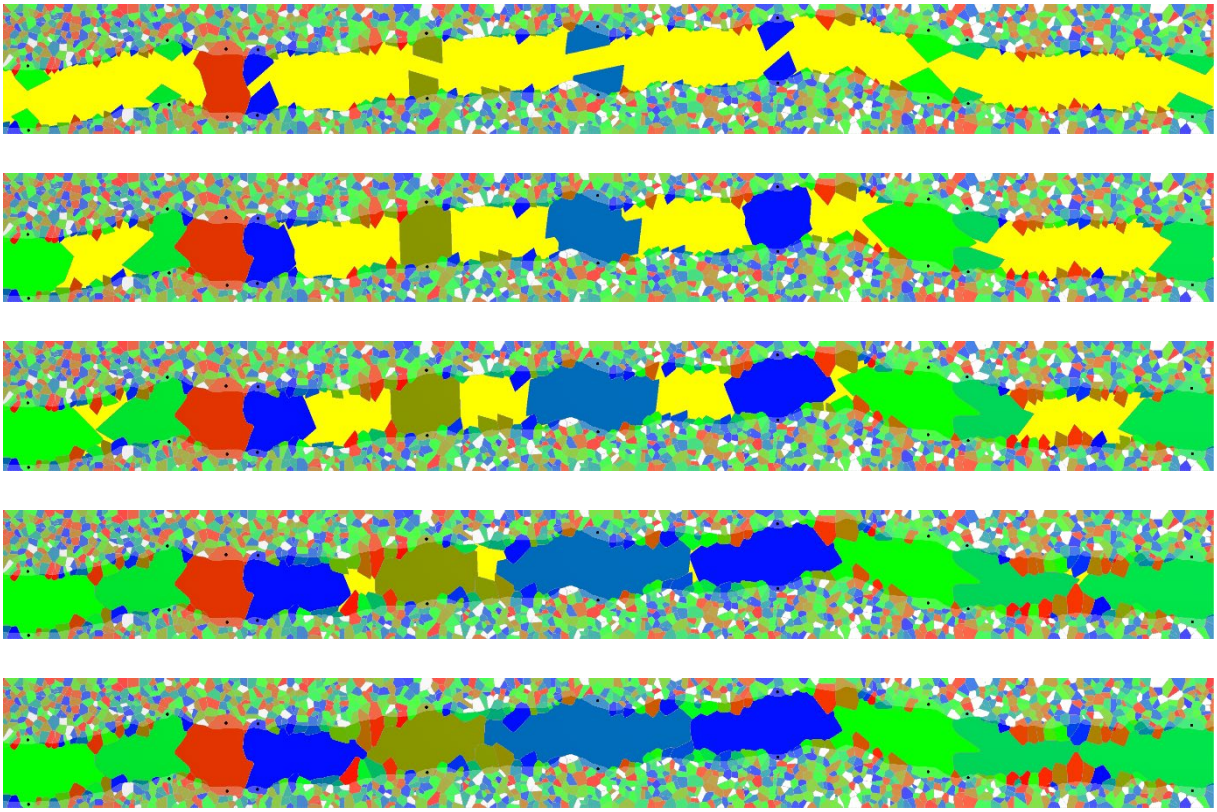

Fracture aperture 12 Dm; ξ=5

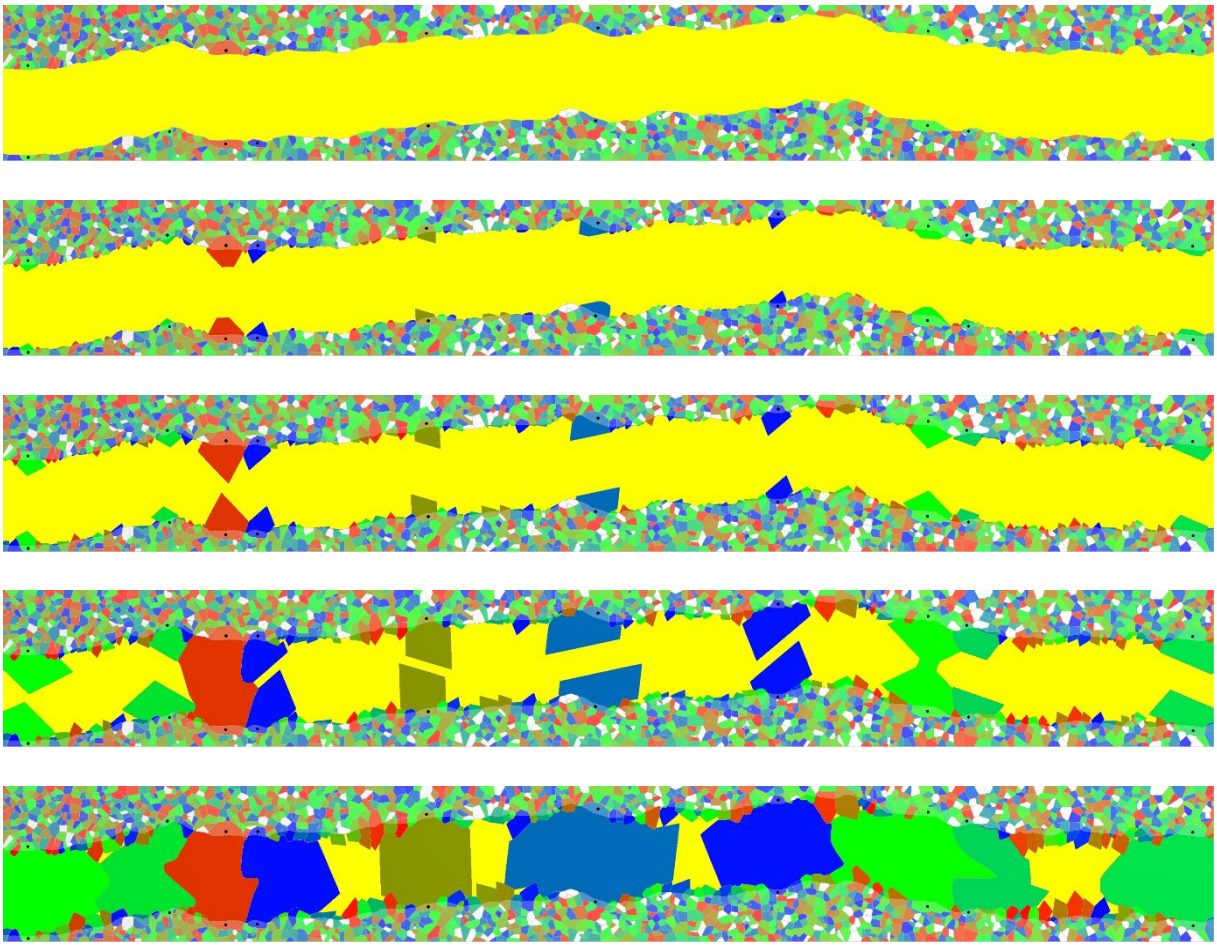

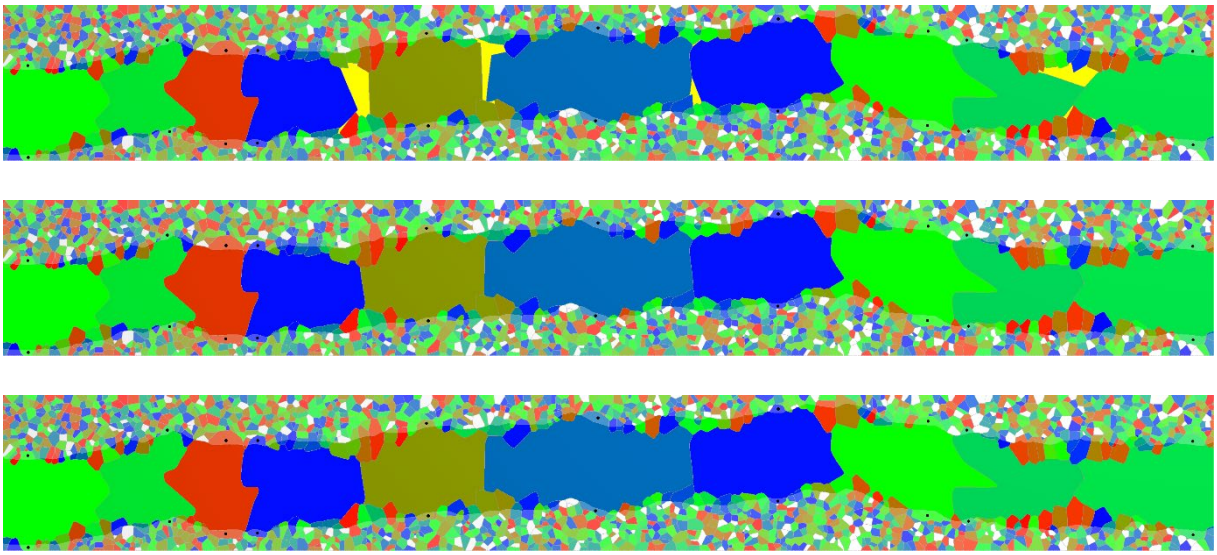

Fracture aperture 16 Dm; ξ=5

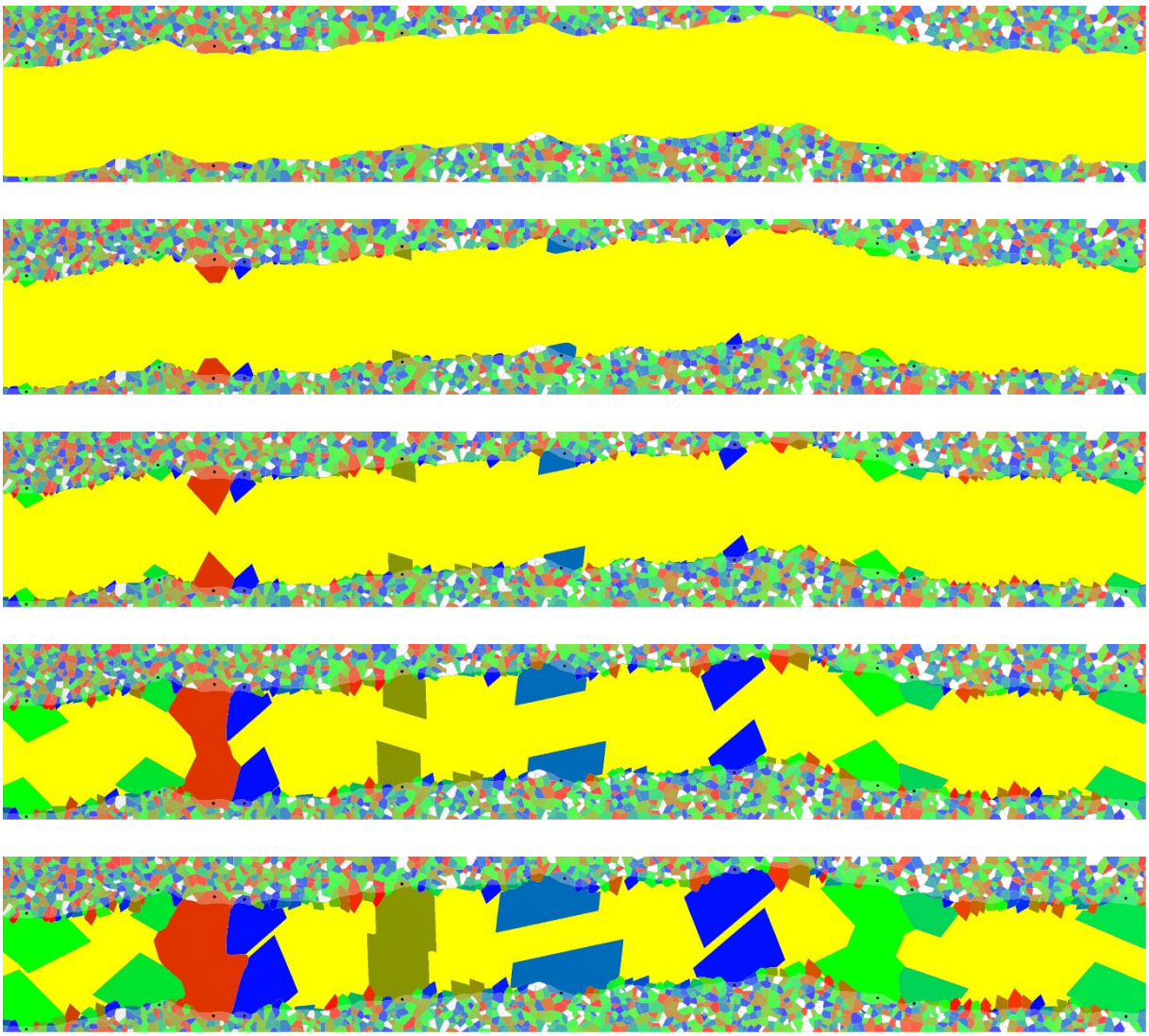

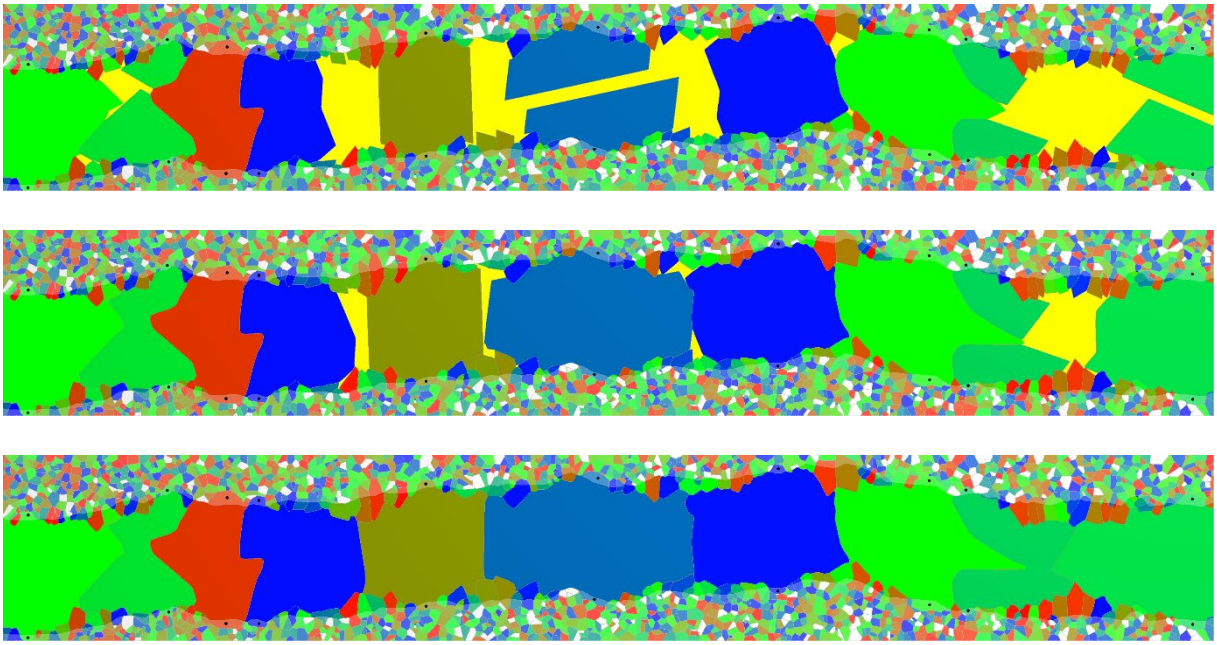

Fracture aperture 1 Dm; ξ=20

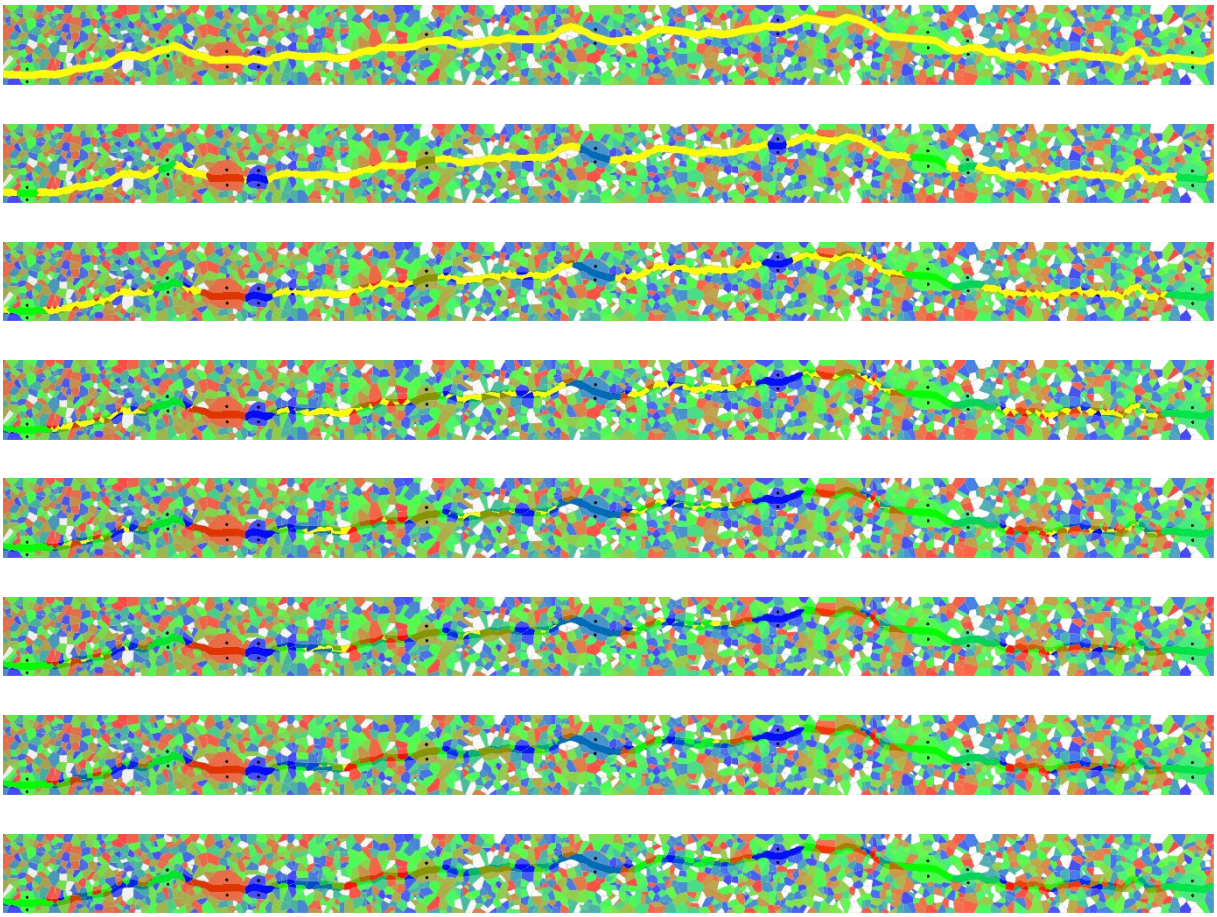

Fracture aperture 2 Dm; ξ=20

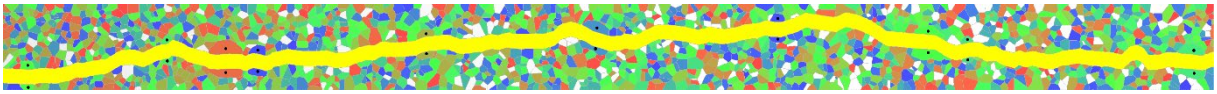

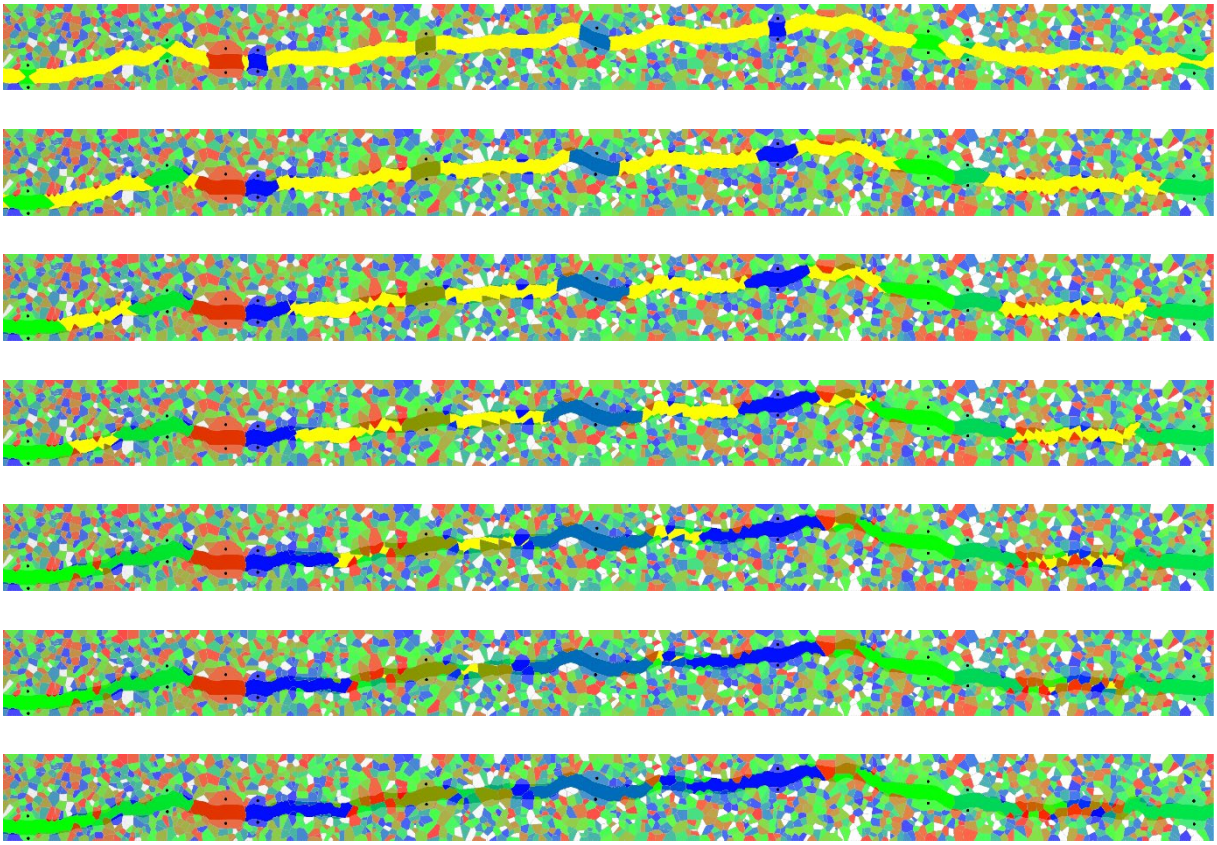

Fracture aperture 4 Dm; ξ=20

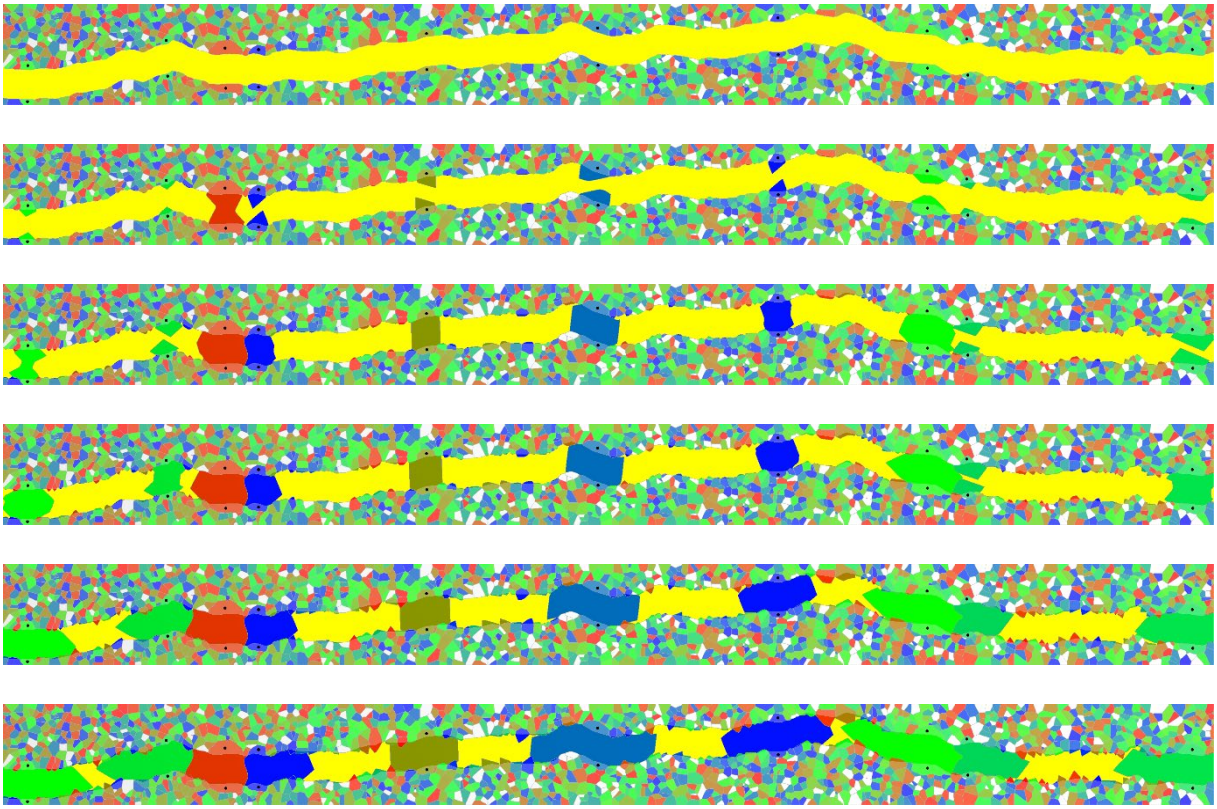

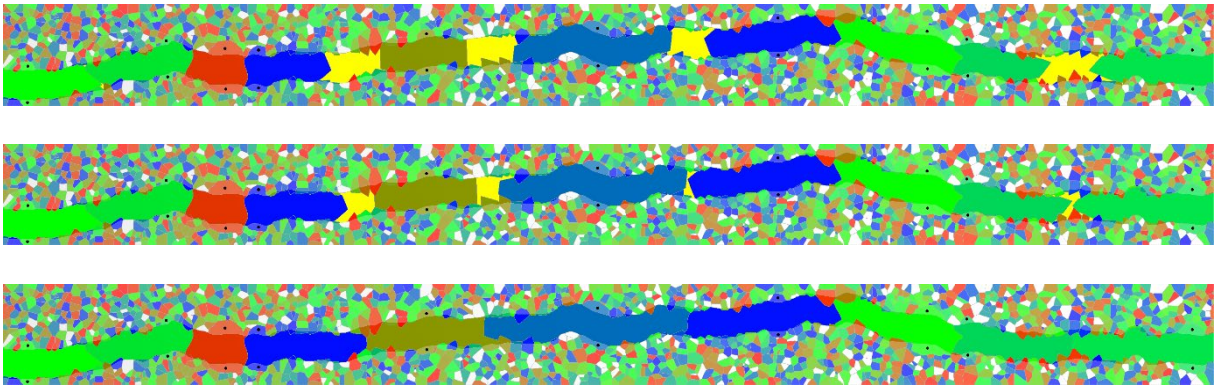

Fracture aperture 8 Dm; ξ=20

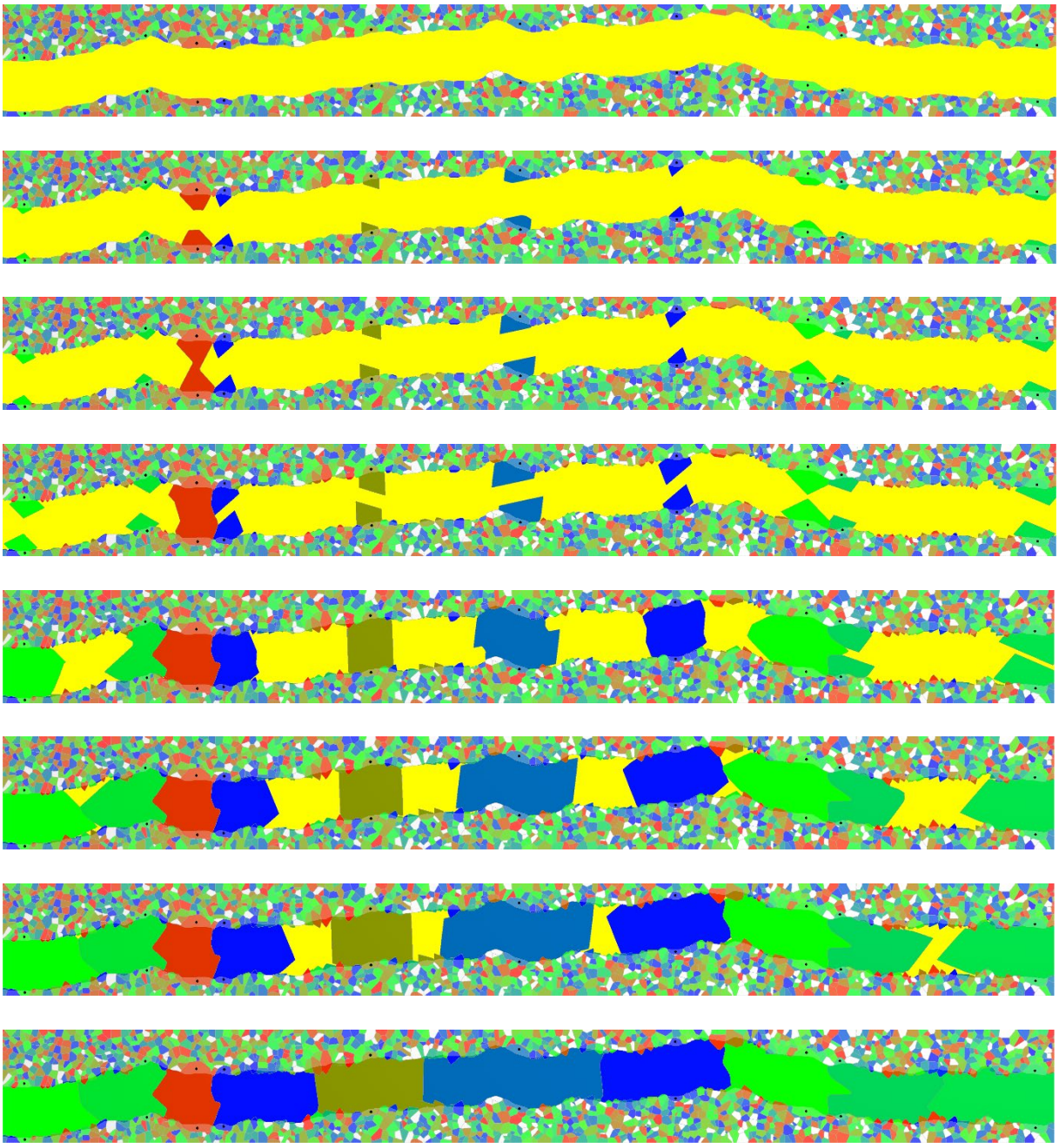

Fracture aperture 12 Dm; ξ=20

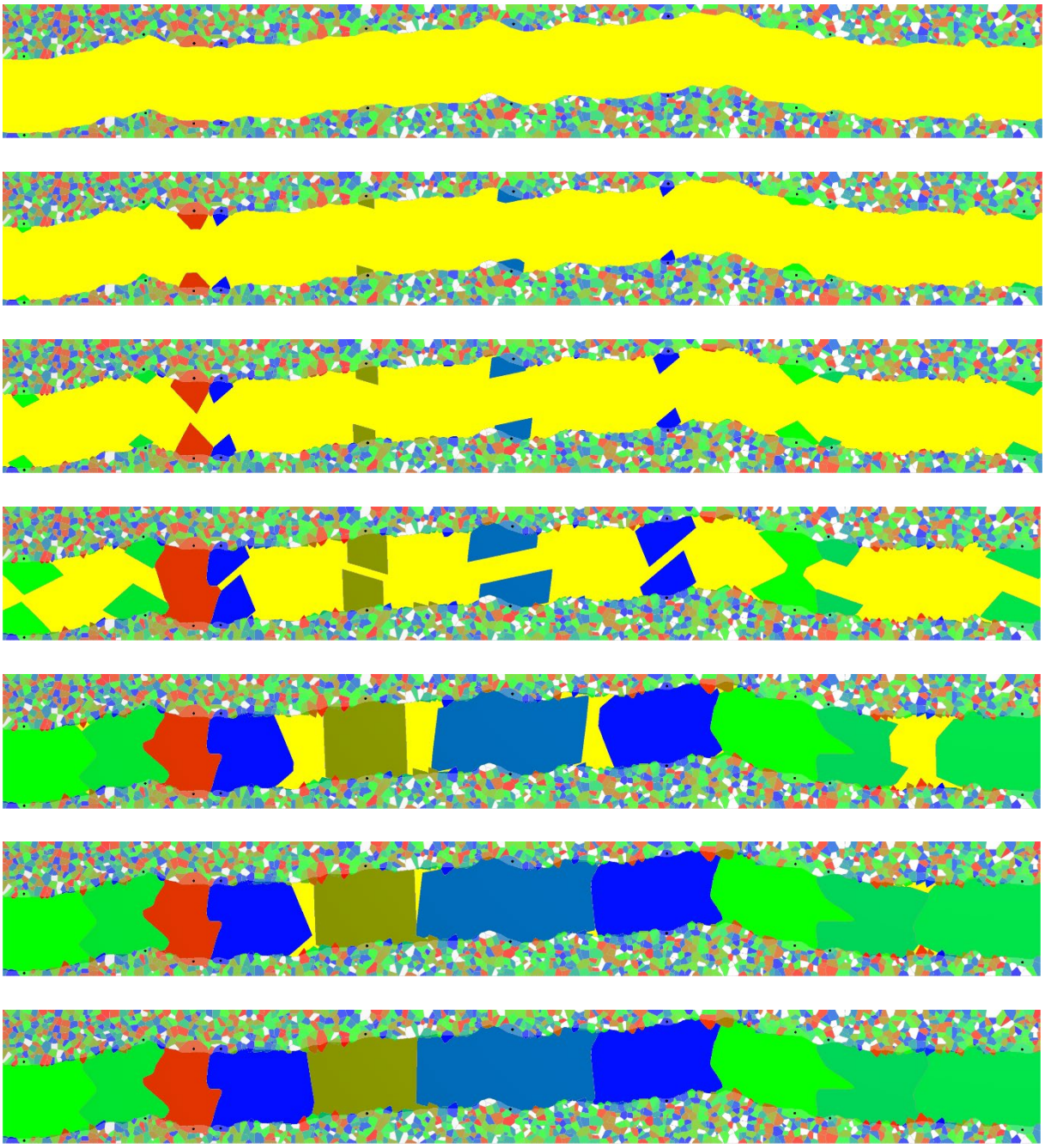

Fracture aperture 16 Dm; ξ=20

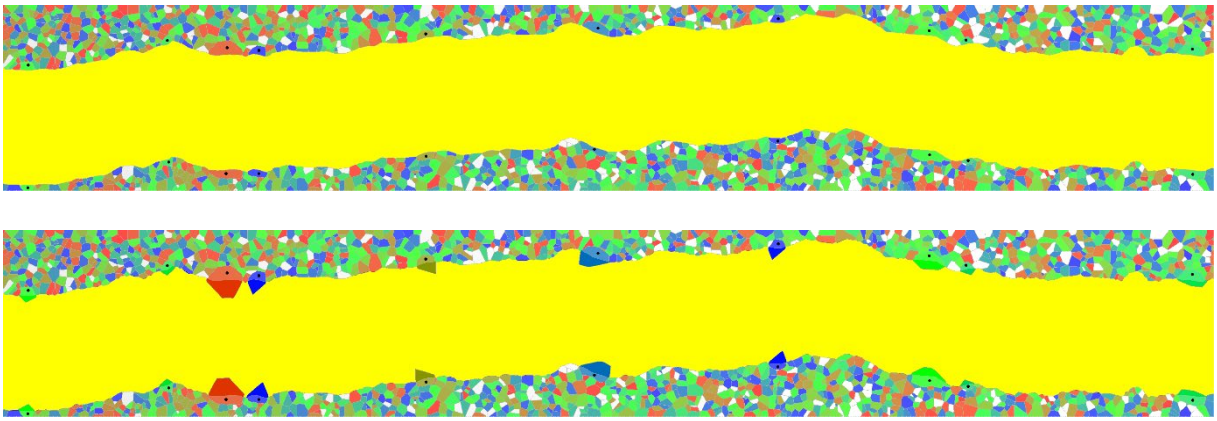

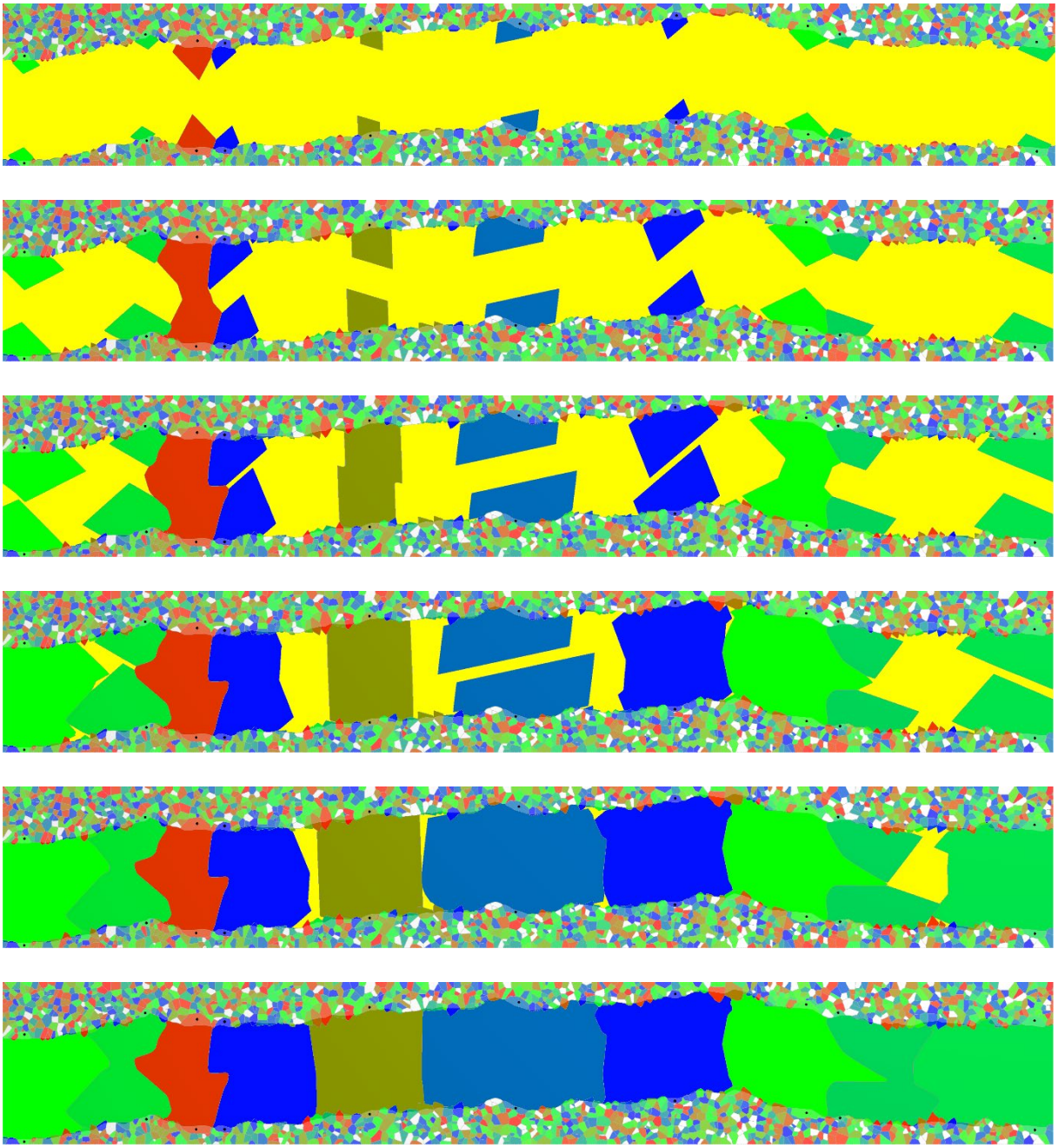

SUPPLEMENT D: 3D RESULTS

We performed 3D simulations in order to illustrate the evolution of vein porosity and permeability during different stages of the fracture filling process. The microstructure along different cross-sectional planes (see Figure DR2C) for apertures of 2, 4, and 8 Dm with different hindering factors and the evolution of the porosity and fluid flow during different stages of filling as well as the grains present at the median line of the veins are depicted in this Supplement.

Fracture aperture 2 Dm; ξ=2.5

3D simulation; cut at ③

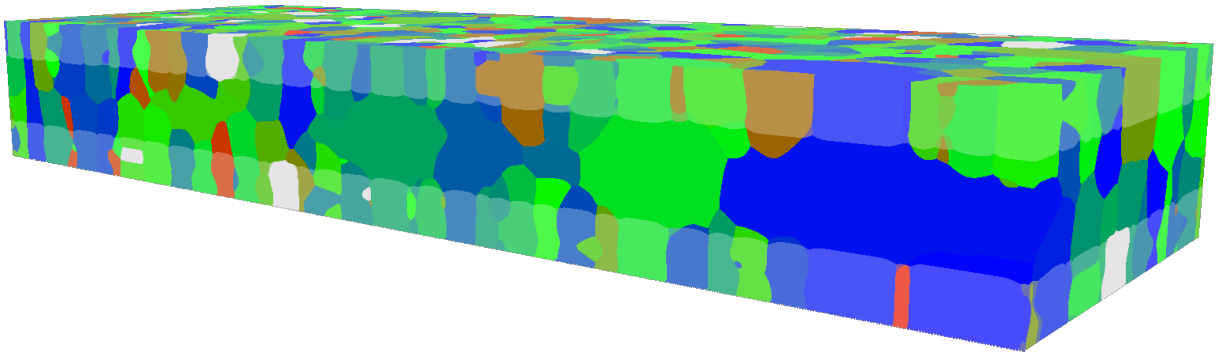

3D simulation; cut at ②

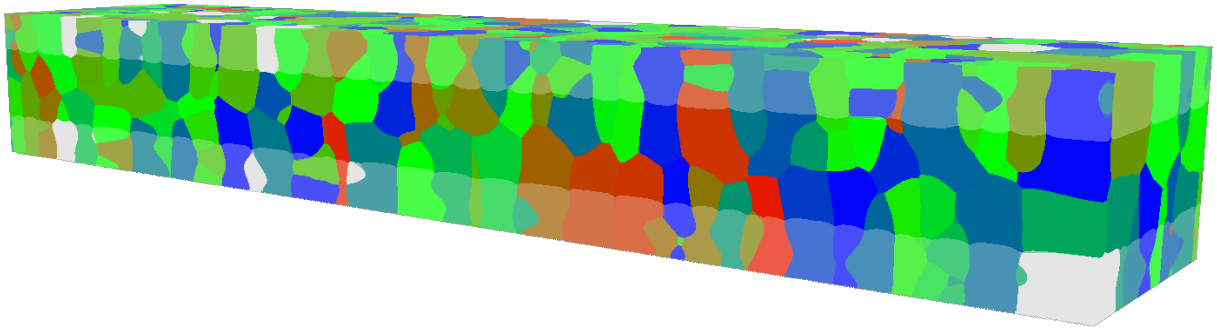

3D simulation; cut at ①

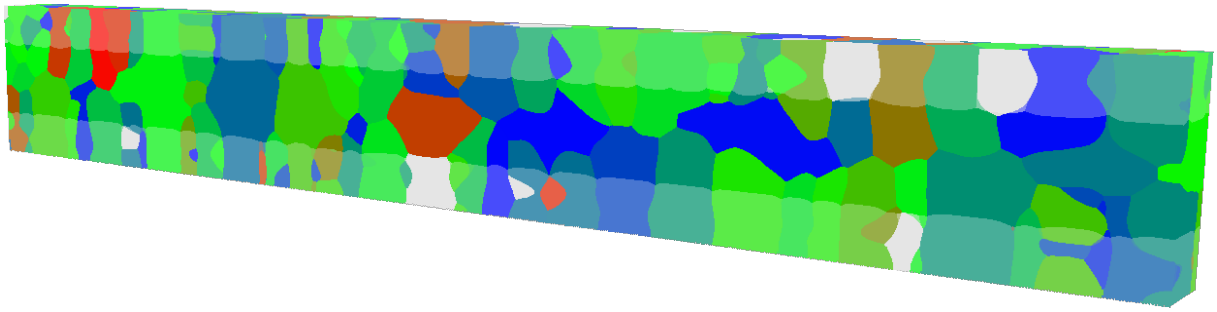

Crystals at the midplane of the vein (yellow = pores)

Step 1

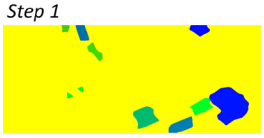

Step 2

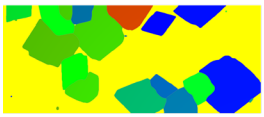

Step 3

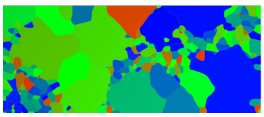

Porosity (blue)

Step 1

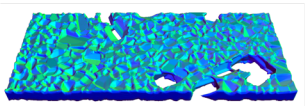

Step 2

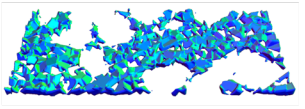

Streamlines (fluid flow simulation)

Step 1

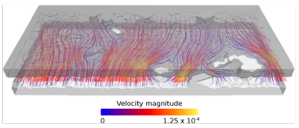

Step 2

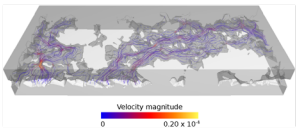

Streamlines (fluid flow simulation)

Step 1

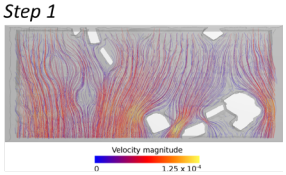

Step 2

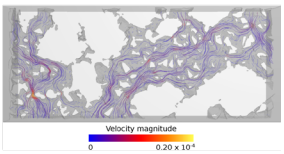

Fracture aperture 2 Dm; ξ=5

3D simulation; cut at ③

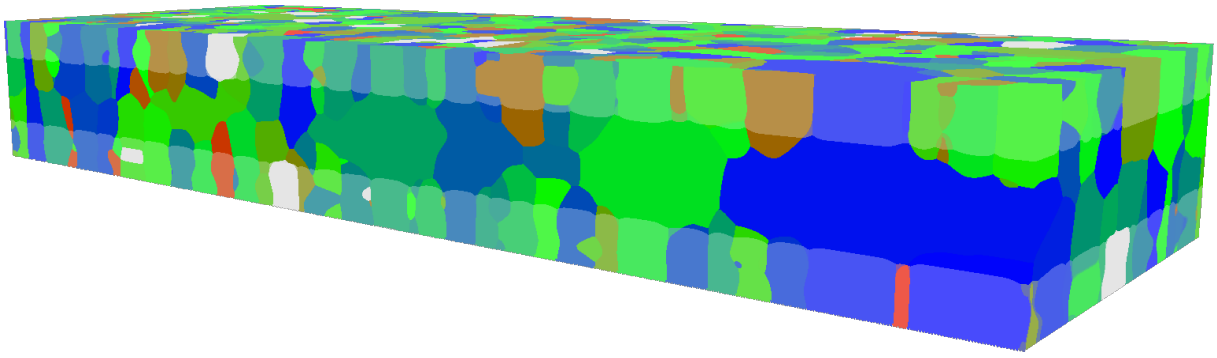

3D simulation; cut at ②

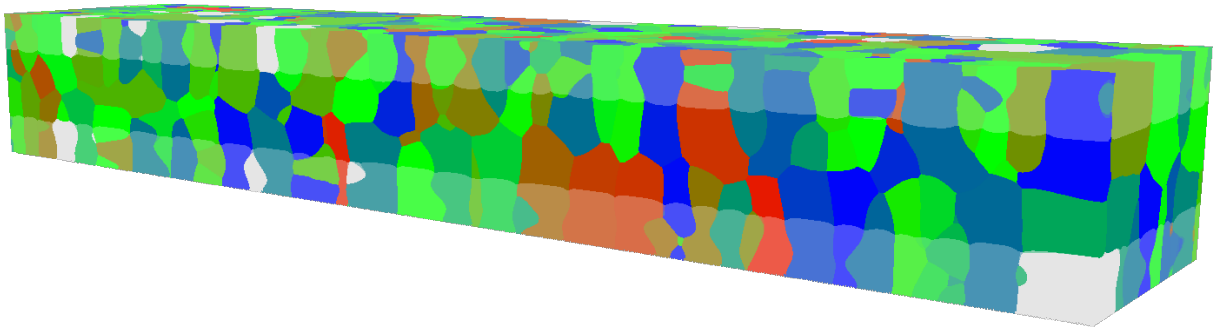

3D simulation; cut at ①

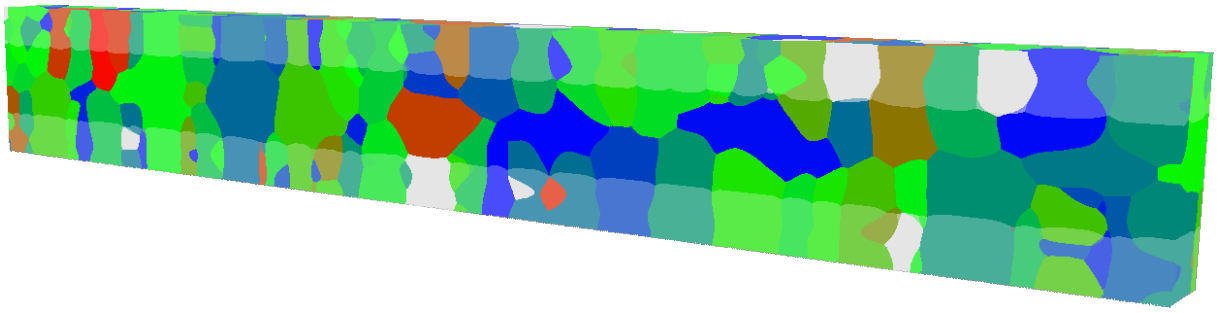

Crystals at the midplane of the vein (yellow = pores)

Step 1

Step 2

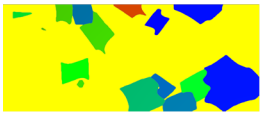

Step 3

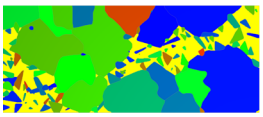

Step 4

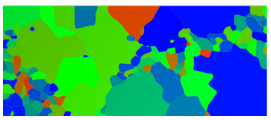

Porosity (blue)

Step 1

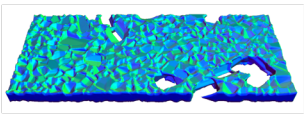

Step 2

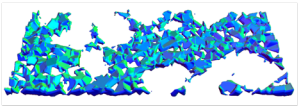

Step 3

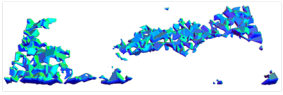

Streamlines (fluid flow simulation)

Step 1

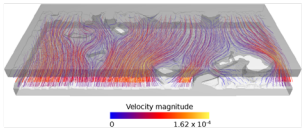

Step 2

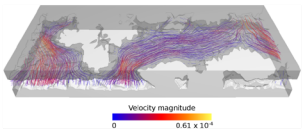

Step 3

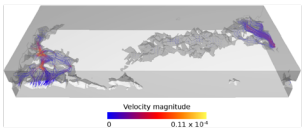

Streamlines (fluid flow simulation)

Step 1

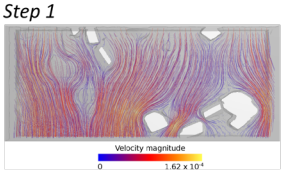

Step 2

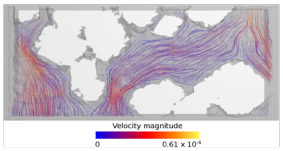

Step 3

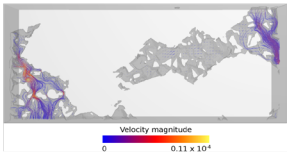

Fracture aperture 4 Dm; ξ=2.5

3D simulation; cut at

③

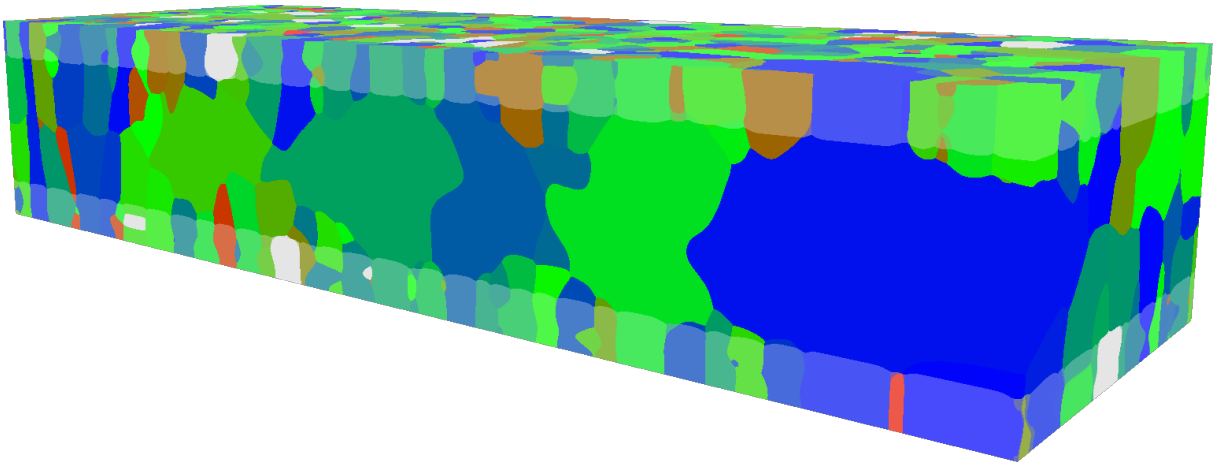

3D simulation; cut at ②

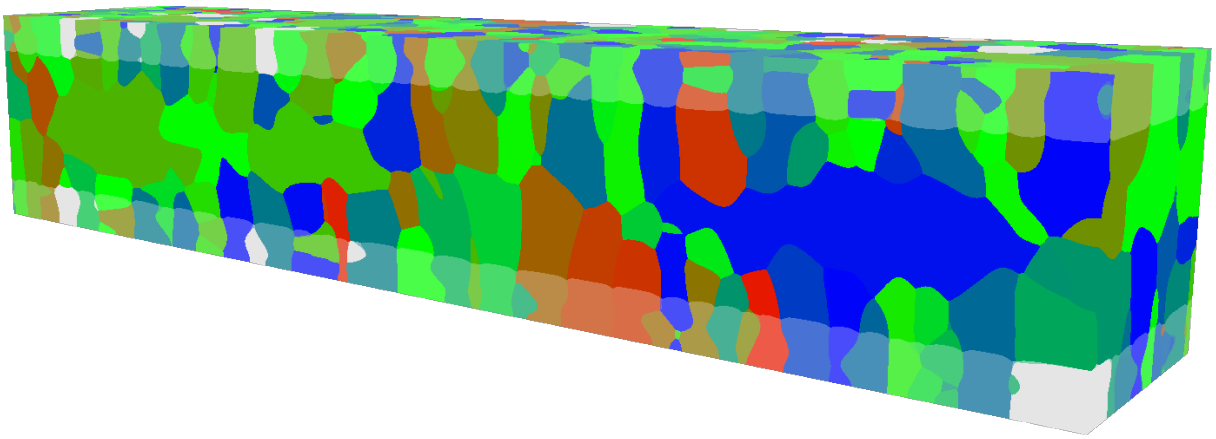

3D simulation; cut at ①

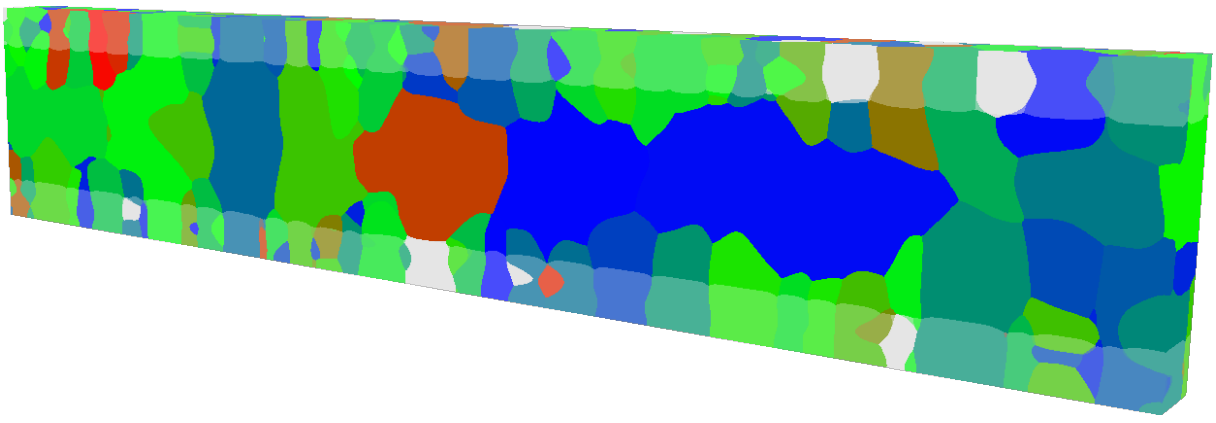

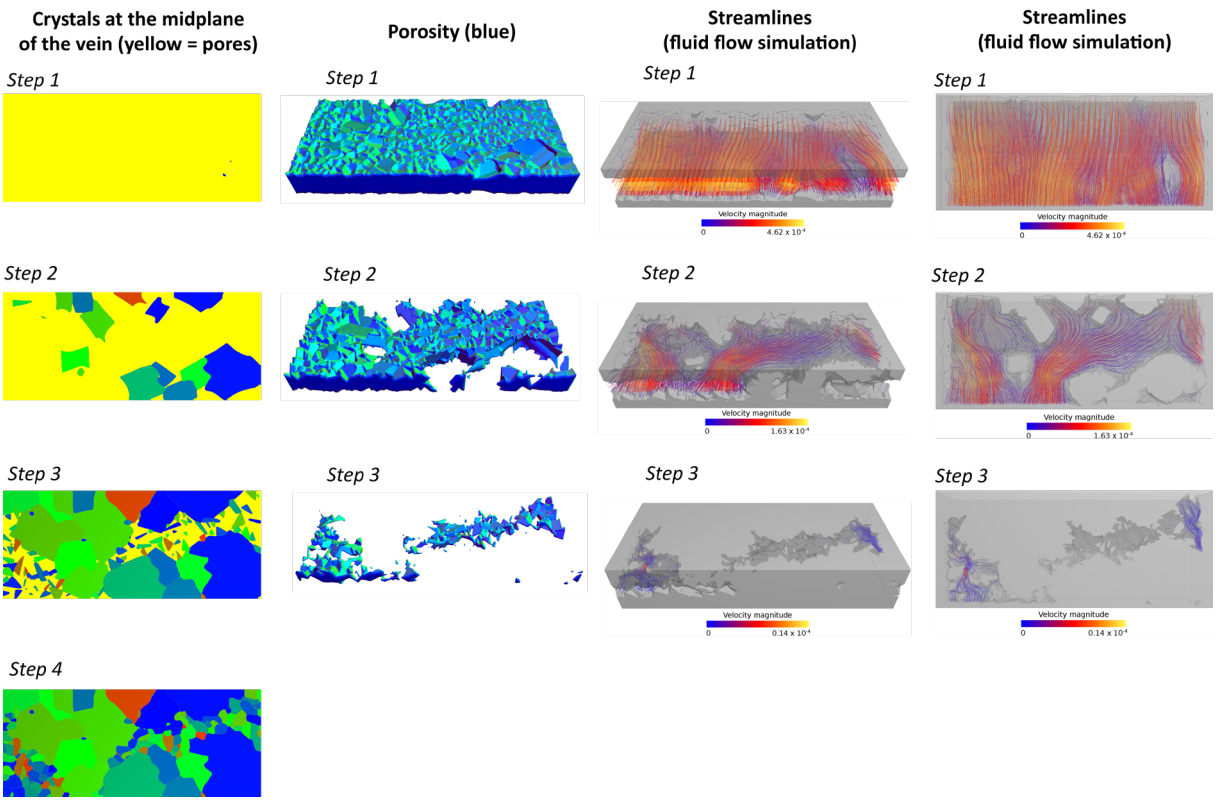
Crystals at the midplane of the vein (yellow = pores)
Porosity (blue)
Streamlines (fluid flow simulation)
Streamlines (fluid flow simulation)
Step 1
Step 2
Step 3
Step 4
Velocity magnitude
0
4.62 x 10⁻⁴
1.63 x 10⁻⁴
0.14 x 10⁻⁴

Fracture aperture 4 Dm; ξ=5

3D simulation; cut at ③

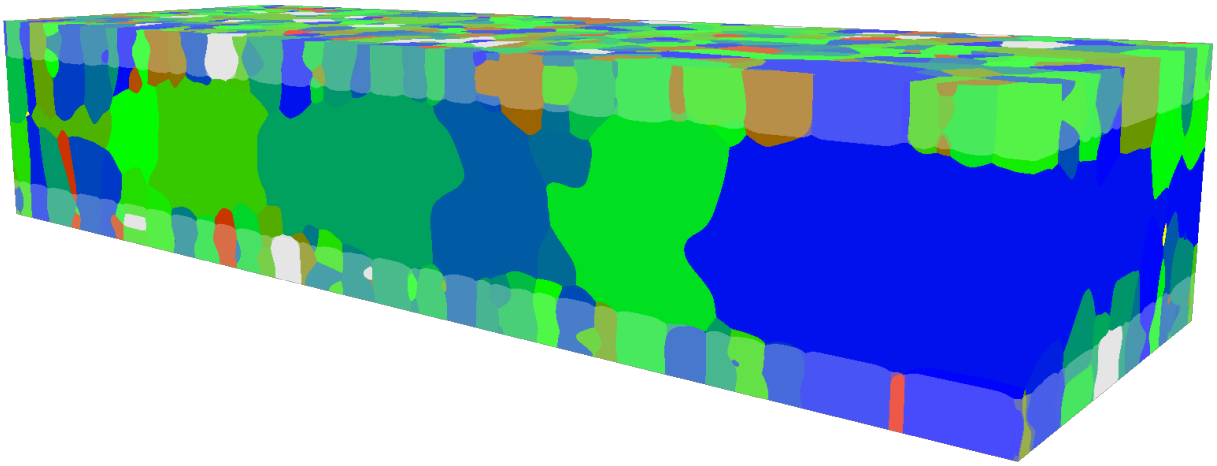

3D simulation; cut at ②

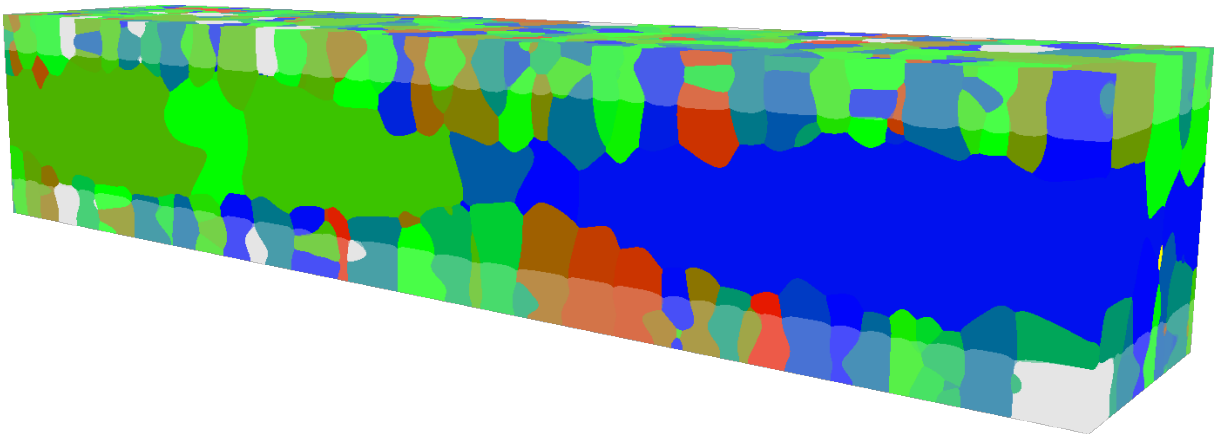

3D simulation; cut at ①

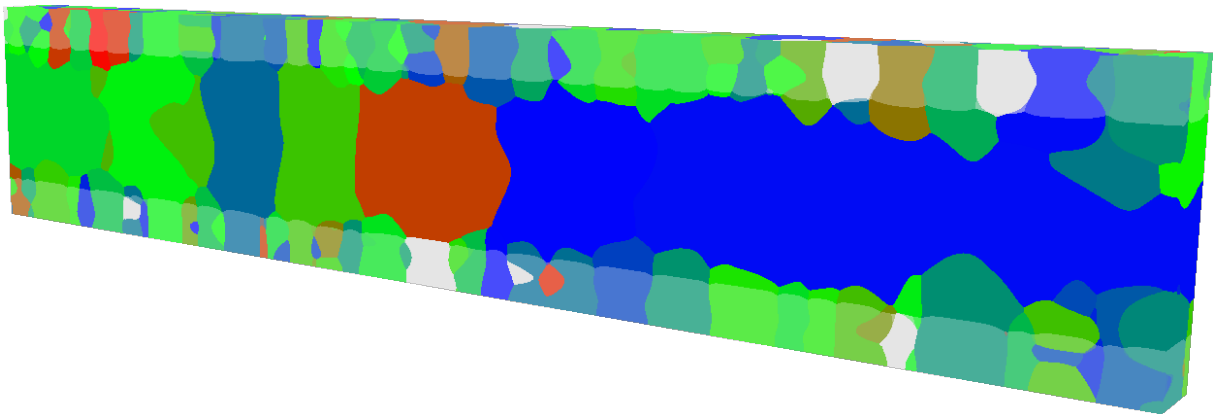

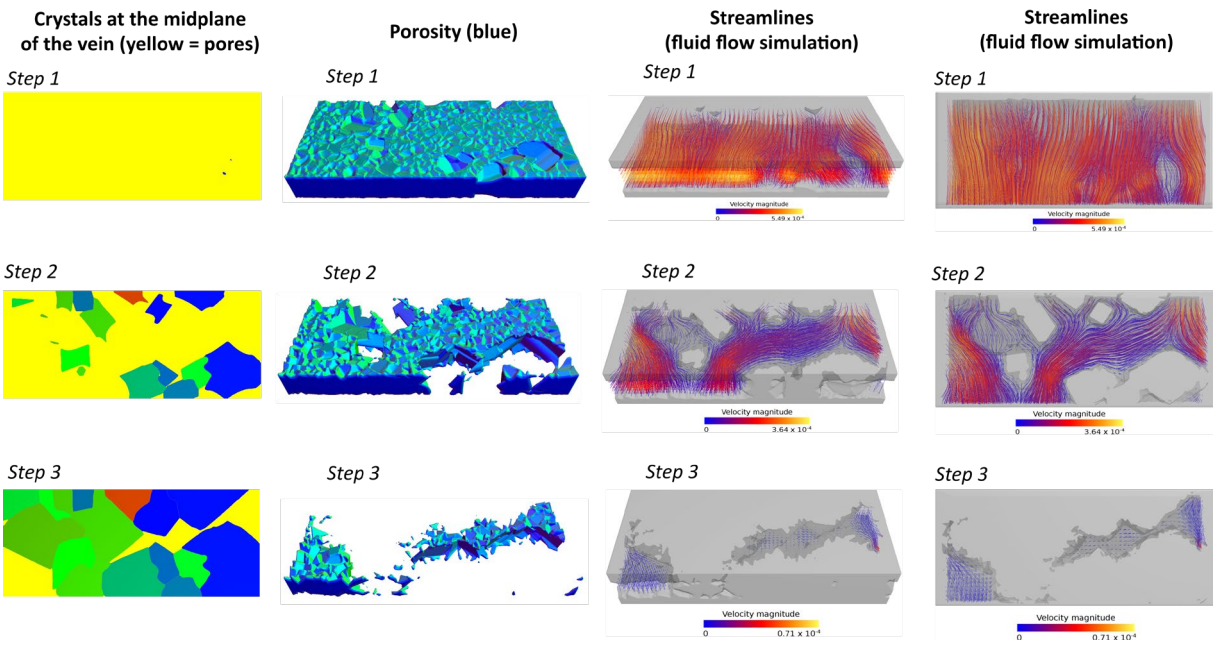
Crystals at the midplane of the vein (yellow = pores)
Porosity (blue)
Streamlines (fluid flow simulation)
Streamlines (fluid flow simulation)
Step 1
Step 2
Step 3
Velocity magnitude
0
5.49 x 10⁻⁴
3.64 x 10⁻⁴
0.71 x 10⁻⁴

Fracture aperture 8 Dm; ξ=5

3D simulation; cut at ③

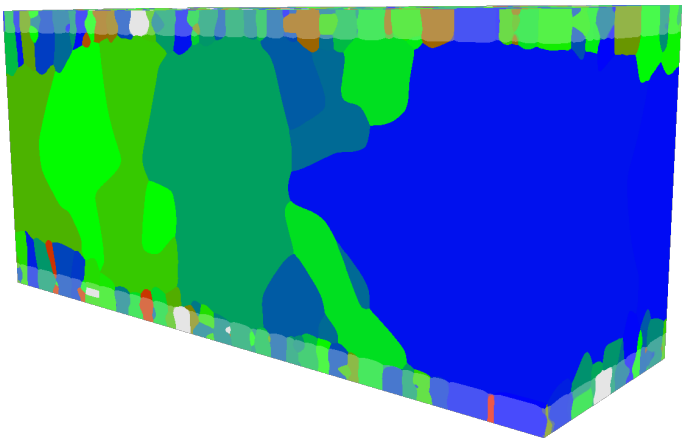

3D simulation; cut at ②

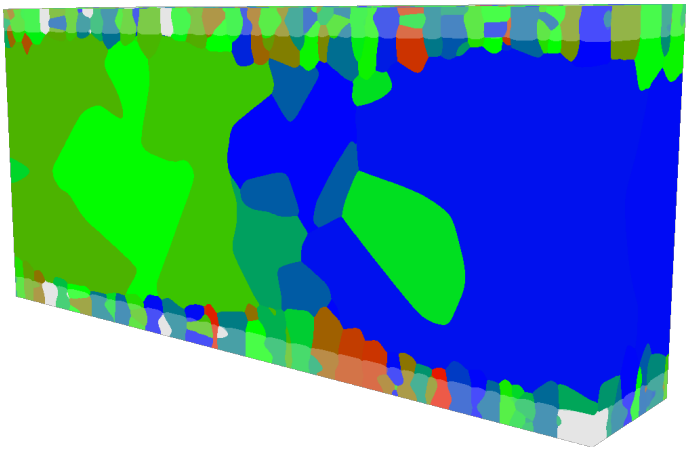

3D simulation; cut at ①

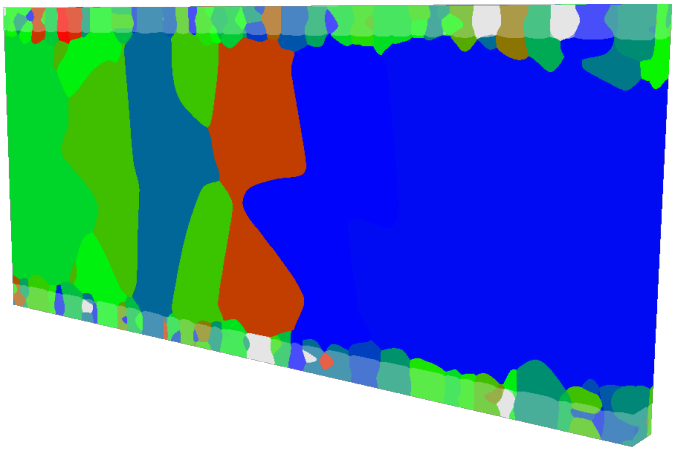

Crystals at the midplane of the vein (yellow = pores)

Step 1

Step 2

Step 3

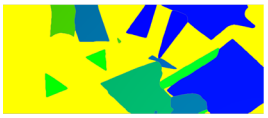

Step 4

Step 5

Porosity (blue)

Step 1

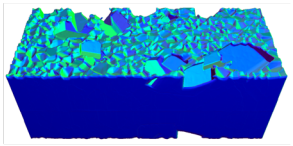

Step 2

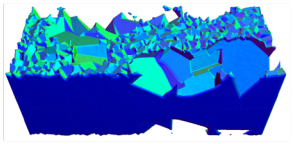

Step 3

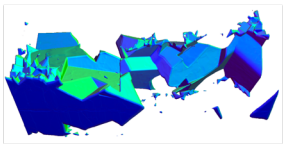

Step 4

Streamlines (fluid flow simulation)

Step 1

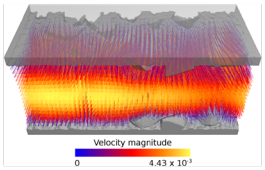

Step 2

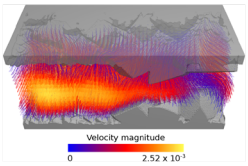

Step 3

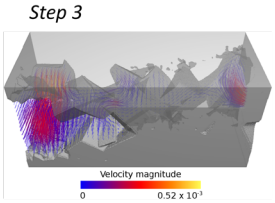

Streamlines (fluid flow simulation)

Step 1

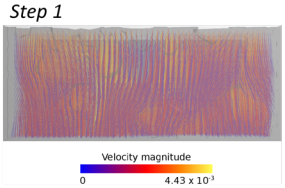

Step 2

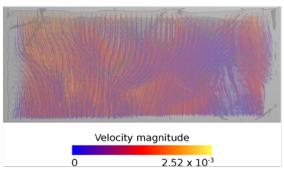

Step 3